Uncovering temporal structure in hippocampal output patterns

Kourosh Maboudi[1, 2†], **Etienne Ackermann**[3†], **Laurel Watkins de Jong**[1, 2], **Brad Pfeiffer**[4], **David Foster**[5], **Kamran Diba**[1,2*†], **Caleb Kemere**[3*†]

[1]Department of Anesthesiology, University of Michigan, Ann Arbor, MI; [2]Department of Psychology, University of Wisconsin-Milwaukee, Milwaukee, WI; [4]Department of Neuroscience, University of Texas Southwestern, Dallas, TX; [5]Department of Psychology and Helen Wills Neuroscience Institute, University of California, Berkeley, CA; [3]Department of Electrical and Computer Engineering, Rice University, Houston, TX

*For correspondence:
kdiba@umich.edu (KD);
caleb.kemere@rice.edu (CK)

[†]These authors contributed equally to this work

Abstract   Place cell activity of hippocampal pyramidal cells has been described as the cognitive substrate of spatial memory. Replay is observed during hippocampal sharp-wave-ripple-associated population burst events (PBEs) and is critical for consolidation and recall-guided behaviors. PBE activity has historically been analyzed as a phenomenon subordinate to the place code. Here, we use hidden Markov models to study PBEs observed in rats during exploration of both linear mazes and open fields. We demonstrate that estimated models are consistent with a spatial map of the environment, and can even decode animals' positions during behavior. Moreover, we demonstrate the model can be used to identify hippocampal replay without recourse to the place code, using only PBE model congruence. These results suggest that downstream regions may rely on PBEs to provide a substrate for memory. Additionally, by forming models independent of animal behavior, we lay the groundwork for studies of non-spatial memory.

Introduction

Large populations of neurons fire in tandem during hippocampal sharp-waves and their accompanying CA1 layer ripple oscillations (*Buzsáki, 1986*). By now, multiple studies have shown that during many sharp-wave ripple-associated population burst events (PBEs), hippocampal "place cells" (*O'Keefe, 1976*) fire in compressed sequences that reflect the firing order determined by the sequential locations of their individual place fields (*Diba and Buzsáki, 2007*; *Foster and Wilson, 2006*; *Lee and Wilson, 2002*; *Nádasdy et al., 1999*). While the firing patterns during active exploration are considered to represent the brain's global positioning system and provide a substrate for spatial and episodic memory, instead it is the synchronized activity during PBEs that is most likely to affect cortical activity beyond the hippocampus (*Buzsáki, 1989*; *Carr et al., 2011*; *Diekelmann and Born, 2010*; *Siapas and Wilson, 1998*). Likewise, widespread activity modulation is seen throughout the brain following these sharp-wave ripple population bursts (*Logothetis et al., 2012*).

The literature on PBEs has largely focused on developing templates of firing patterns during active behavior and evaluating the extent to which these templates' patterns are reprised during subsequent PBEs. But what if the fundamental mode of the hippocampus is not the re-expression of place fields, but rather the PBE sequences during sharp-wave ripples (SWRs)? PBE sequences are enhanced during exploration of novel environments (*Cheng and Frank, 2008*; *Foster and Wilson, 2006*), they presage learning-related changes in place fields (*Dupret et al., 2010*), and appear to be critical to task learning (*Ego-Stengel and Wilson, 2010*; *Girardeau et al., 2009*; *Jadhav et al., 2012*).

42   Here, we examine the information provided by CA1 and CA3 pyramidal neurons, the output nodes
43   of the hippocampus, through the looking glass of PBE firing patterns.
44   We developed a technique to build models of PBE sequences strictly outside of active exploration
45   and independent of place fields and demonstrate that this nevertheless allows us to uncover spatial
46   maps. Furthermore, these models can be used to detect congruent events that are consistent
47   with replay but without any explicit place cell template. Our technique therefore provides new
48   possibilities for evaluating hippocampal output patterns in single-trial and other fast learning
49   paradigms, where a reliable sequential template pattern is not readily available. Overall, our work
50   suggests that a sequence-first approach can provide an alternative view of hippocampal activity
51   that may shed new light on how memories are formed, stored, and recalled.

Results

Awake population burst events

54   We began by analyzing the activity of large numbers of individual neurons in areas CA1 and CA3
55   of the dorsal hippocampus as rats navigated linear mazes for water reward (linear track: $n = 3$
56   rats, $m = 18$ sessions; previously used by *Diba and Buzsáki* (*2007*)). Using pooled multiunit activity,
57   we detected PBEs during which many neurons were simultaneously active. The majority of these
58   events occurred when animals paused running (speed < 5 cm/s, corresponding to $54.0\% \pm 20.1\%$ sd
59   of events) to obtain reward, groom, or survey their surroundings (*Buzsáki et al., 1983*), and were
60   accompanied by SWR complexes, distinguished by a burst of oscillatory activity in the 150–250 Hz
61   band of the CA1 local field potential (LFP). Because we are interested in understanding internally
62   generated activity during PBEs, we included only these periods without active behavior, ensuring
63   that theta sequences would not bias our results. While we identified active behavior using a speed
64   criterion, we found similar results when we instead used a theta-state detection approach (not
65   shown). We did not add any other restrictions on behavior, LFPs, or the participation of place cells.
66   We found that inactive PBEs occupied an average of 1.8% of the periods during which animals were
67   on the linear track (16.9 ± 15.1 s of 832.6 ± 390.5 s). In comparison, classical Bayesian approaches to
68   understand PBE activity require the 34.8% of time animals are running (speed > 10 cm/s) on the
69   track (254.4 ± 106.6 s of 832.6 ± 390.5 s) to build models of place fields.

Learning hidden Markov models from PBE data

71   Activity during PBEs is widely understood to be internally-generated in the hippocampal-entorhinal
72   formation, and likely to affect neuronal firing in downstream regions (*Buzsáki, 1989*; *Chrobak and
73   Buzsáki, 1996*; *Logothetis et al., 2012*; *Yamamoto and Tonegawa, 2017*). Given the prevalence of
74   PBEs during an animal's early experience, we hypothesized that the neural activity during these
75   events would be sufficient to train a machine learning model of sequential patterns—a hidden
76   Markov model—and that this model would capture the relevant spatial information encoded in the
77   hippocampus independent of exploration itself.
78   Hidden Markov models have been very fruitfully used to understand sequentially structured
79   data in a variety of contexts. A hidden Markov model captures information about data in two
80   ways. First, it clusters observations into groups ("states") with shared patterns. In our case, this
81   corresponds to finding time bins in which the same sets of neurons are co-active. This is equivalent
82   to reducing the dimension of the ensemble observations into a discretized latent space or manifold.
83   Second, it models the dynamics of state transitions. This model is Markovian because it is assumed
84   that the probability to transition to the next state only depends on the current state. Critically,
85   these operations of clustering and sequence modeling are jointly optimized, allowing the structure
86   of ensemble firing corresponding to each of the final states to combine information over many
87   observations. Given the role of the hippocampus in memory, in our hidden Markov models (HMMs),
88   the unobserved latent variable presumably corresponds to the temporal evolution of a memory
89   trace that is represented by co-active ensembles of CA1 and CA3 neurons. The full model will
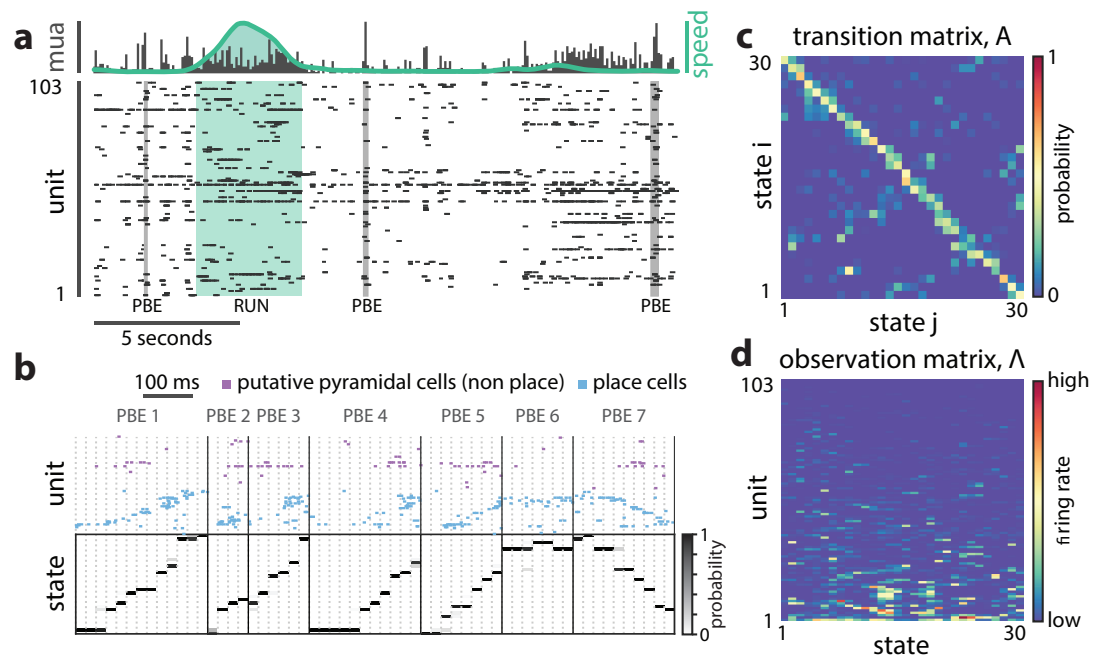
Figure 1. A hidden Markov model of ensemble activity during population burst events. **a.** Examples of three PBEs and a run epoch. **b.** Spikes during 7 example PBEs (top) and their associated (30 state HMM-decoded) latent space distributions (bottom). The place cells are ordered by their place fields on the track, whereas the non-place cells are unordered. The latent states are ordered according to the peak densities of the latent-state place fields (lsPFs, see Materials and Methods). **c.** The transition matrix models the dynamics of the unobserved internally-generated state. The sparsity and banded-diagonal shape are suggestive of sequential dynamics. **d.** The observation model of our HMM is a set of Poisson probability distributions (one for each neuron) for each hidden state. Looking across columns (states), the mean firing rate is typically elevated for only a few of the neurons and individual neurons have elevated firing rates for only a few states.

Figure 1–Figure supplement 1. Hidden Markov models capture state dynamics beyond pairwise co-firing.

90   correspond to the structure which connects all the memory traces activated during PBEs.

91   The parameters of our model that are fit to data include the observation model (the cluster
92   descriptions, or predicted activity of each excitatory neuron within the CA1/CA3 ensemble for a
93   given state), the state transition model (the probability that the CA1/CA3 ensemble will transition
94   from a start state to a destination state in the next time bin), and the initial state distribution (the
95   probability for sequences to start in each given state). In prior work using HMMs to model neural
96   activity, a variety of statistical distributions have been used to characterize ensemble firing during a
97   specific state (the observation model, *Chen and Wilson* (*2017*); *Chen et al.* (*2012*, 2014); *Deppisch*
98   *et al.* (*1994*); *Kemere et al.* (*2008*); *Radons et al.* (*1994*). We opted for the Poisson distribution to
99   minimize the number of parameters per state and per neuron (see Materials and Methods). We
100   used the standard iterative expectation-maximization (EM) algorithm (*Rabiner, 1989*) to learn the
101   parameters of an HMM from binned PBE data (20 ms bins). *Figure 1* depicts the resultant state
102   transition matrix and observation model for an example linear-track session.

103   Using separate training- and test-datasets (cross-validation) mitigates over-fitting to training
104   data, but it is still possible for the cross-validated goodness-of-fit to increase with training without
105   any underlying dynamics, e.g., if groups of neurons tend to activate in a correlated fashion. Does the
106   model we have learned reflect underlying sequential structure of memory traces beyond pairwise
107   co-firing? To answer this question, we cross-validated the model against both real "test" data
108   and against surrogate "test" data derived from shuffling each PBE in two ways: one in which the
109   binned spiking activity was circularly permuted across time for each neuron independently of the
110   other neurons ("temporal shuffle", which removes co-activation), and one in which the order of
111   the binned data was scrambled coherently across all neurons ("time-swap", which maintains co-

112 activation). Note that the second shuffle preserves pairwise correlations while removing the order
113 of any sequential patterns that might be present. Using five-fold cross-validation, we compared
114 learned models against both actual and surrogate test data and found that the model likelihood
115 was significantly greater for real data (vs. temporal shuffle, $p < 0.001$, vs. time-swap, $p < 0.001$, $n = 18$
116 sessions, Wilcoxon signed-rank test, *Figure 1–Figure Supplement 1*).

What do the learned model parameters tell us about PBEs?

118 To begin to understand what structure we learn from PBE activity, we compared our HMMs (trained
119 on real data) against models trained on multiple different surrogate datasets (*Figure 2*a,b). These
120 surrogate datasets were obtained from actual data following: 1) temporal shuffles and 2) time-
121 swaps, as above, and 3) by producing a surrogate PBE from independent Poisson simulations
122 according to each unit's mean firing rate within the original PBEs. First, we investigated the sparsity
123 of the transition matrices using the Gini coefficient (see Materials and Methods and *Figure 2–Figure
124 Supplement 1*). A higher Gini coefficient corresponds to higher sparsity. Strikingly, the actual data
125 yielded models in which the state transition matrix was sparser than in each of the surrogate
126 counterparts ($p < 0.001$, *Figure 2*c), reflecting that each state transitions only to a few other states.
127 Thus, intricate yet reliable details are captured by the HMMs. Next, we quantified the sparsity of the
128 observation model. We found that actual data yielded mean firing rates which were highly sparse
129 (*Figure 2*d), indicating that individual neurons were likely to be active during only a small fraction
130 of the states. Using a graph search algorithm (see Materials and Methods), we simulated paths
131 through state space generated by these transition matrices, and found that this increased sparsity
132 accompanied longer trajectories (*Figure 2–Figure Supplement 3*) through the state space of the
133 model. Thus, the state transition matrices we learn are suggestive of dynamics in which each sparse
134 state is preceded and followed by only a few other, in turn, sparse states, providing long sequential
135 paths through state space-consistent with spatial relationships in the environment in which the
136 animal was behaving, but generated from PBEs. The increased sparsity of the observation model
137 and transition matrix in the example session was representative of a significant increase over all
138 remaining sessions ($p < 0.05$, $n = 18$ sessions, Wilcoxon signed-rank tests, *Figure 2*e,f).

139 These observations indicate that PBEs inform an HMM about extant spatial relationships within
140 the environment. So, next we asked how the firing patterns of neurons during actual behavior
141 project into the learned latent spaces. To observe the evolution of the latent states during behavior,
142 we used our model to determine the most likely sequence of latent states corresponding to decode
143 the neural activity observed in 100 ms bins during epochs that displayed strong theta oscillations
144 (exclusive of PBEs) when rats were running (speed > 10 cm/s; see Materials and Methods). If the
145 learned model was distinct from ensemble patterns during behavior, we might expect the resulting
146 state space probability distributions at each point in time to be randomly spread among multiple
147 states. Instead, we found distributions that resembled sequential trajectories through the latent
148 space (*Figure 3*a) in parallel with the physical trajectories made by the animal along the track, further
149 demonstrating that the latent state dynamics learned from PBEs corresponds to an internalized
150 model of physical space.

151 To better understand the relationship between the latent space and physical space, we used
152 the latent state trajectories decoded during running to form an estimate of the likelihood of each
153 state as a function of location on the track (see Materials and Methods). These "latent-state
154 place fields" (lsPFs, *Figure 3*b) in many ways resembled neuronal place fields and similarly tiled
155 the extent of the track. This spatial localization went away when we re-estimated the lsPFs with
156 shuffled positions (*Figure 3*c). To quantify how informative the latent states were about position,
157 we used the lsPFs to map decoded state sequences to position during running periods (*Figure 3*d).
158 In our example session, decoding through the latent space resulted in a median accuracy of 5 cm,
159 significantly greater than the 47 cm obtained from shuffled lsPFs ($p < 0.001$, Wilcoxon signed-rank
160 test, *Figure 3*d). When we evaluated decoding error over our full set of sessions, we observed a
161 similar result ($p < 0.001$, Wilcoxon signed-rank test, *Figure 3*e, *Figure 3–Figure Supplement 1*). As
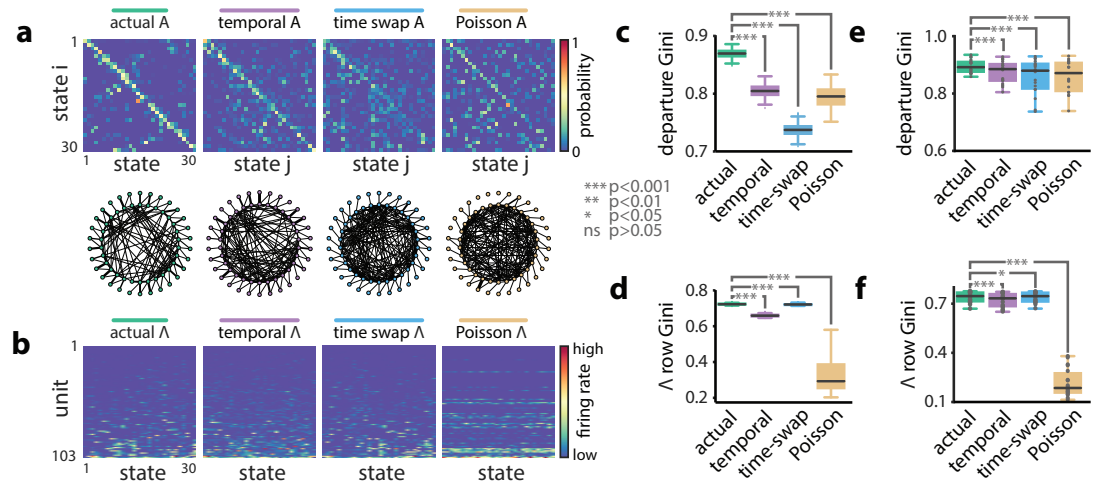
Figure 2. Models of PBE activity are sparse. We trained HMMs on neural activity during PBEs (in 20 ms bins), as well as on surrogate transformations of those PBEs. **a.** (top) The transition matrices for the actual and surrogate PBE models with states ordered to maximize the transition probability from state i to state $i + 1$. (bottom) Undirected connectivity graphs corresponding to the transition matrices. The nodes correspond to states (progressing clockwise, starting at the top). The weights of the edges are proportional to the transition probabilities between the nodes (states). The transition probabilities from state i to every other state except $i + 1$ are shown in the interior of the graph, whereas for clarity, transition probabilities from state i to itself, as well as to neighboring state $i + 1$ are shown between the inner and outer rings of nodes (the nodes on the inner and outer rings represent the same states). **b.** The observation matrices for actual and surrogate PBE models show the mean firing rate for neurons in each state. For visualization, neurons are ordered by their firing rates. **c.** We quantified the sparsity of transitions from one state to all other states using the Gini coefficient of rows of the transition matrix for the example session in **a.**. Actual data yielded sparser transition matrices than shuffles. **d.** The observation models—each neuron's expected activity for each state—learned from actual data for the example session are significantly sparser than those learned after shuffling. This implies that as the hippocampus evolves through the learned latent space, each neuron is active during only a few states. **e.** Summary of transition matrix sparsity and **f.** Observation model sparsity with corresponding shuffle data pooled over all sessions/animals. (***: $p < 0.001$, *: $p < 0.05$; single session comparisons: $n = 250$ realizations, Welch's t-test; aggregated comparisons - $n = 18$ sessions, Wilcoxon signed-rank test).

Figure 2–Figure supplement 1. PBE model states typically only transition to a few other states.

Figure 2–Figure supplement 2. Each neuron is active in only a few model states.

Figure 2–Figure supplement 3. The sparse transitions integrate into long sequences through the state space.
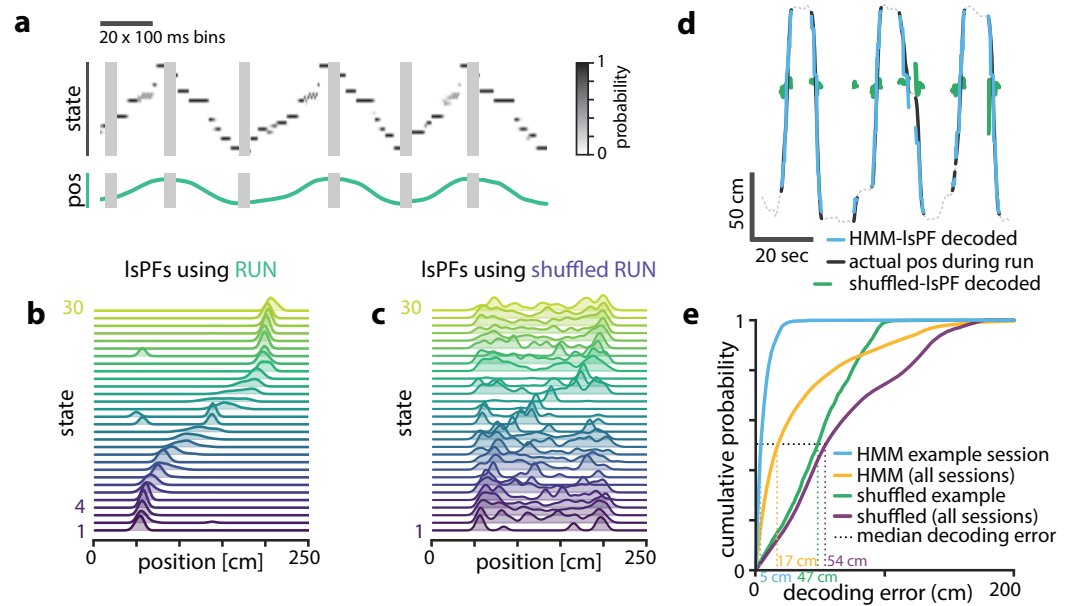
Figure 3. Latent states capture positional code. **a.** Using the model parameters estimated from PBEs, we decoded latent state probabilities from neural activity during periods when the animal was running. An example shows the trajectory of the decoded latent state probabilities during six runs across the track. **b.** Mapping latent state probabilities to associated animal positions yields latent-state place fields (lsPFs) which describe the probability of each state for positions along the track. **c.** Shuffling the position associations yields uninformative state mappings. **d.** For an example session, position decoding during run periods through the latent space gives significantly better accuracy than decoding using the shuffled tuning curves. The dotted line shows the animal's position during intervening non run periods. **e.** The distribution of position decoding accuracy over all sessions ($n = 18$) was significantly greater than chance. ($p < 0.001$).

Figure 3–Figure supplement 1. Latent states capture positional code over wide range of model parameters.

our method required discretizing the state space, a potential caveat is that the number of latent states is a relevant parameter, which we arbitrarily chose to be 30. However, latent-state place fields were informative of position over a wide range of values of this parameter (*Figure 3–Figure Supplement 1*). Note that decoding into the latent space and then mapping to position resulted in slightly higher error than simply performing Bayesian decoding on the neural activity during behavior. This suggests that the latent space we learn from PBEs may not capture all the information about space that is present in hippocampal activity during behavior, though this may also reflect the limited number of PBEs from which we can learn.

HMM-congruent PBEs capture sequence replay

We and others have previously described how the pattern of place cell firing during many PBEs recapitulates the order in which they are active when animals run on the track (*Figure 4*a). We employed the versatile and widely-used Bayesian decoding method to ascribe a replay score to sequential patterns during PBEs. Briefly, for each PBE, we used place-field maps to estimate a spatial trajectory (an *a posteriori* distribution of positions) in 20 ms bins. We generated surrogate data via a column-cycle shuffle (i.e., a circular shift across positions for each time bin (*Davidson et al., 2009*)) of the *a posteriori* distributions during PBEs. The real and surrogate trajectories were scored (see Materials and Methods), and we defined replay events as those for which the score of the actual trajectory was larger than a threshold fraction of the null distribution generated by the surrogate scores. Using this approach, we found that 57% of PBEs (1064 of 1883) were identified as replay beyond a threshold of 99% (median across datasets 54.2%, interquartile range = 32.8–61.0%, *Figure 4–Figure Supplement 1*). Thus, as has been reported many times (*Davidson et al., 2009*; *Diba*

and Buzsáki, 2007; *Foster and Wilson, 2006*; *Karlsson and Frank, 2009*), only a fraction of PBEs (but many more than expected by chance) represent statistically significant replay. Given that we use all PBEs for model learning and our models capture the structure of the environment and the patterns expressed by place cells during exploration, we were interested in understanding whether we could also use our latent-space models to find these replay events. Indeed, for many events when we decode trajectories through state space, they resemble the sequential patterns observed when we decode position using Bayesian techniques and the place cell map (*Figure 4*b, left). However, given previous evidence for replay of environments not recently experienced (*Gupta et al., 2010*; *Karlsson and Frank, 2009*), we hypothesized that some PBEs might contain ensemble neural activity which is unstructured and thus unrelated to the learned model, and that these would correspond to the "non-replay" events found using traditional methods.

To assess how well the pattern of ensemble activity during individual PBEs related to the overall state-space model learned from PBE activity ("congruence"), we developed a statistical approach for identifying the subset of strongly structured PBEs. Specifically, rather than comparing real and surrogate PBEs, we compared the goodness-of-fit for each event to a null distribution generated via a computationally-efficient manipulation of the transition matrix of the model (*Figure 4*b); we row-wise shuffled the non-diagonal elements of the transition matrix to assess whether an individual PBE is a more ordered sequence through state space than would be expected by chance. Maintaining the diagonal avoids identifying as different from chance sequences which consist of few repeated states, marked by transitions between state i and itself. As described above, the fraction of events identified as replay using Bayesian decoding is strongly tied to how the null-distribution is generated (i.e., what shuffle is used), some secondary criteria (e.g., number of active cells, unit cluster quality, peak firing rate, trajectory "jumps", etc.), and the value of the significance threshold arbitrarily chosen to be 90%, 95%, or 99% of shuffles in different reports. When we combined across datasets, we found that our transition matrix shuffle yielded a null distribution for which a 99% confidence interval identified slightly fewer PBEs as significant than the column-cycle shuffle did for Bayesian decoding (*Figure 4*c). To make a principled comparison of Bayesian- and HMM-based replay detection schemes, we fixed the Bayesian-based significance threshold at 99% but selected the significance threshold for the HMM-congruence null distribution so that the fraction of replay events detected would be the same between the two schemes. Following this approach, we found that model-congruent/incongruent PBEs largely overlapped with the replay/non-replay events detected using Bayesian decoding of the place cell map (*Figure 4*d). Thus, using only the neural activity during PBEs, without access to any place cell activity, we are remarkably able to detect the sequential patterns typically described as "replay" based only on their consistency with the structure of other PBE activity.

There were, however, also differences between the Bayesian and HMM-congruent approaches, including events that reached significance in one but not the other formalism. We wanted to understand where and why these approaches differed in identifying significant sequences. When we examined individual PBEs, we found sequences for which both Bayesian and model-congruence replay detection approaches appeared to malfunction (*Figure 5*a). This was not a failure of the choice of significance threshold, as for both techniques we found what appeared to be false-negatives (patterns which looked like replay but were not significant) as well as false-positives (patterns which looked noisy but were identified as replay). Thus, in order to quantitatively compare the two approaches, we asked eight humans to visually examine all the PBEs in our database. They were instructed to label as replay PBEs in which the animal's Bayesian decoded position translated sequentially without big jumps (*Silva et al., 2015*, see Materials and Methods).

We marked each event as a "true" community replay if it was identified by a majority of scorers (six individuals scored $n = 1883$ events, two individuals scored a subset of $n = 1423$ events, individual scores are shown in *Figure 5–Figure Supplement 1*). We calculated an receiver operating charac-teristic (ROC) curve which compared the rate of true positive and false positive detections as the significance thresholds for Bayesian and model-congruence approaches were varied (*Figure 5*b). A
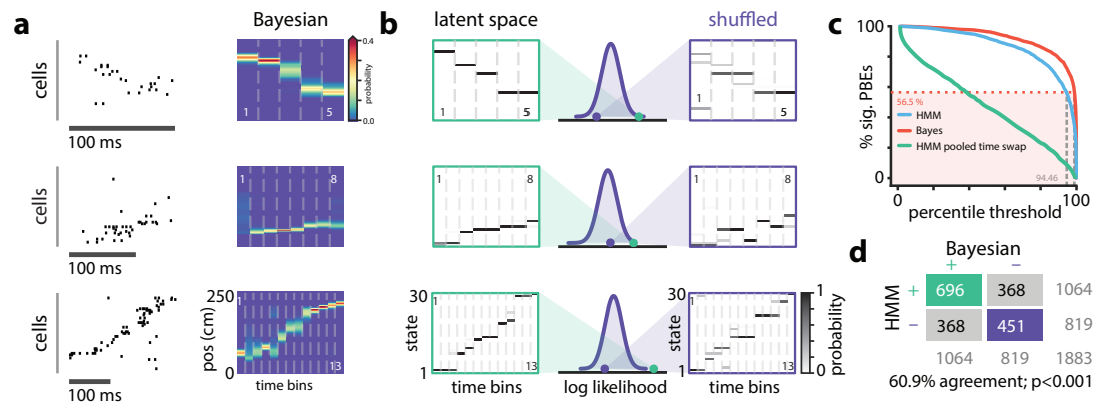
Figure 4. a. Example PBEs decoded to position using Bayesian decoding. **b.** (left) Same examples decoded to the latent space using the learned HMM. (right) Examples decoded after shuffling the transition matrix, and (middle) the sequence likelihood using actual and shuffled models. **c.** Effect of significance threshold on the fraction of events identified as replay using Bayesian decoding and model congruent events using the HMM approach. **d.** Comparing Bayesian and model-congruence approaches for all PBEs recorded, we find statistically significant agreement in event identification (60.9% agreement, $n = 1883$ events from 18 sessions, $p < 0.001$, Fisher's exact test two sided).

Figure 4–Figure supplement 1. Number of significant PBEs.

perfect detector would have an area under the curve (AUC) of unity. We did not find a significant difference between the AUCs of Bayesian decoding and model-congruence ($p = 0.14$, bootstrap, see Methods). If we select thresholds such that our algorithms yield a similar fraction of significant vs. total events as the 24% denoted by our human scorers, we find that both Bayesian and model-congruence yield agreement of $\approx 70\%$ labeled events with each other and with human scorers (*Figure 5*c).

Thus, congruence with an HMM trained only on PBEs appears to work as reliably as Bayesian decoding in detecting sequential reactivation of linear track behaviors. However, when we examined individual sessions, we noticed that performance was quite variable. Given that our models are learned only from PBEs, we reasoned that the statistics or structure of the PBEs within each session might yield models which vary in quality depending on the number of recorded units, the number of PBEs detected, and their self-consistency across events. We created a model quality metric by comparing cross-validated learning statistics to models which were learned from shuffled events (see Materials and Methods). We found that the performance of model-congruence detection was tied to model quality ($R^2 = 0.17$, $F = 2.9$, $n = 18$ sessions, *Figure 5–Figure Supplement 1*). Model quality, in turn, was highly correlated with the number of PBEs during the session ($R^2 = 0.96$, $F = 392.6$, $n = 18$ sessions, *Figure 5–Figure Supplement 1*). Not surprisingly, the performance of Bayesian decoding relative to human scorers was independent of the quality of the HMM, or the number of PBEs, as the place field model is learned from ensemble neural activity during running. Thus, we find an intriguing contrast—when there is an abundance of PBEs (indicating novelty, learning, hippocampus-dependent planning, etc.(*Buzsáki, 2015*)), even in the absence of repeated experience, replay detection based on PBE activity is highly effective. Conversely, when there are few PBEs (i.e., scenarios in which PBEs are uncorrelated with cognitive function), but an abundance of repeated behavioral trials, Bayesian decoding of these limited events proves more effective.

Modeling internally generated activity during open field behavior

The linear track environment represents a highly-constrained behavior. We therefore asked whether the hidden Markov model approach could generalize to more complex environments and behavioral tasks. *Pfeiffer and Foster* (*2013*, 2015) had previously recorded activity of CA1 neurons in rats as they explored in a 2 m × 2 m open field arena for liquid reward. Briefly, animals were trained to discover which one of 36 liquid reward wells would be the "home" well on a given day. They then
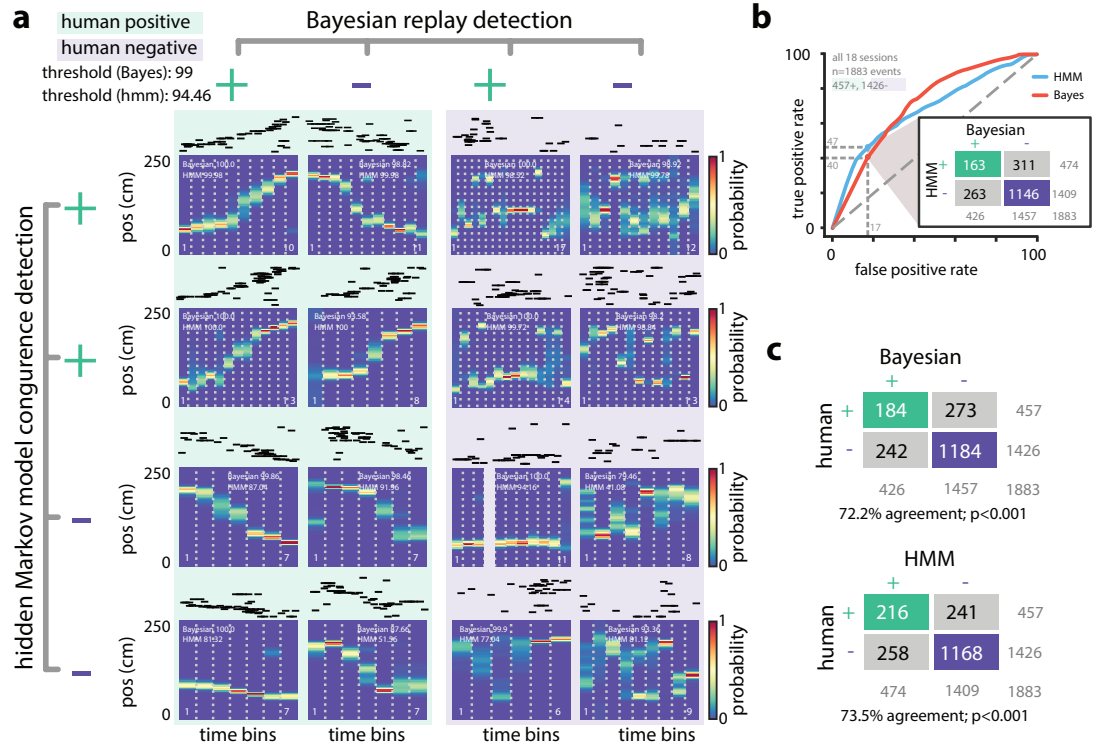
Figure 5. a. Eight examples from one session show that Bayesian decoding and HMM model-congruence can differ in labeling of significant replay events. For each event, spike rasters (ordered by the location of each neuron's place field) and the Bayesian decoded trajectory are shown. "+" ("-") label corresponds to significant (insignificant) events. (left) Both methods can fail to label events that appear to be sequential as replay and (right) label events replay that appear non-sequential. **b.** We recruited human scorers to visually inspect Bayesian decoded spike trains and identify putative sequential replay events. Using their identifications as labels, we can define an ROC curve for both Bayesian and HMM model-congruence which shows how detection performance changes as the significance threshold is varied. (inset) Human scorers identify 24% of PBEs as replay. Setting thresholds to match this value results in agreement of 70% between Bayesian and HMM model-congruence. **c.** Using the same thresholds, we find $\approx 70\%$ agreement between algorithmic and human replay identification. (All comparison matrices, $p < 0.001$, Fisher's exact test two-tailed.)

**Figure 5–Figure supplement 1.** Human scoring of PBEs and session quality.

264 were required to alternate between searching for a randomly rewarded well and returning to the
265 home well. Using the place cell map in this task and Bayesian decoding, many PBEs were decoded
266 to trajectories through two-dimensional space that were predictive of behavior and shaped by
267 reward. Using this same dataset, we trained a HMMs on neural activity during PBEs in the open field.
268 Here, we used the same PBEs detected previously (*Pfeiffer and Foster, 2013*, *2015*) which occupied
269 an average of $2.53 \pm 0.42\%$ of the periods during which animals were behaving (77.91 ± 21.16 s out
270 of 3064.86 ± 540.26 s). Given the large number of units available in this dataset and the increased
271 behavioral variability in the open field environment compared to the linear track, we chose to
272 estimate HMMs with 50 latent states. The transition matrix and observation model from a sample
273 session are shown in *Figure 6*a,b. Despite the complex and varied trajectories displayed by animals,
274 the HMM captured sequential dynamics in PBE activity, as in the 1D case, when we compared
275 learned models against both actual and surrogate test data, we found that the model likelihood
276 was significantly greater for real data ($p < 0.001$, Wilcoxon signed-rank test).

277 In the case of the linear track, we linked sparsity of the transition matrix to the sequential nature
278 of behaviors in that environment. An unconstrained, two-dimensional environment permits a much
279 richer repertoire of behavioral trajectories. However, behavior is still constrained by the structure of
280 space—arbitrary teleportation from one location to another is impossible. We found that learning
281 from PBEs in the open field yielded transition matrices (*Figure 6*a) that were significantly sparser
282 than models learned from shuffled data ($p < 0.05$, Wilcoxon signed-rank test, $n = 8$ sessions,
283 *Figure 5–Figure Supplement 1*). However, consistent with increased freedom of potential behaviors,
284 when we compared the sparsity of models learned from open field PBEs with 50-state models
285 learned from PBEs in linear tracks, the open field transition matrices were less sparse ($p < 0.001$,
286 Mann–Whitney *U* test comparing 8 and 18 sessions, *Figure 4–Figure Supplement 1*). Likewise,
287 when we examined the observation model for the open field, we found that the activity across
288 states for individual neurons was significantly more sparse than in models learned from shuffled
289 data ($p < 0.05$, Wilcoxon signed-rank test, $n = 8$ sessions, *Figure 6–Figure Supplement 1*). The
290 sparsity of linear track and open field observation models were not significantly different ($p = 0.44$,
291 Mann–Whitney *U* test).

292 Do the latent states learned from PBEs capture spatial information in a 2D environment? We
293 used the PBE-trained model to decode run data, as in the linear track case. We found that the latent
294 states corresponded with specific locations in the open field, as we expected (*Figure 6*c). Moreover,
295 we were able to decode animals' movements with significantly greater than chance accuracy by
296 converting decoded latent states to positions using the lsPF ($p < 0.001$, *Figure 6*d). Finally, we
297 examined model-congruency for PBEs detected in the open field. Previously, it was reported that
298 27.3% (815 of 2980, $n = 8$ sessions) were identified as "trajectory events" (*Pfeiffer and Foster,*
299 *2015*). We chose a significance threshold to match this fraction (*Figure 6–Figure Supplement 3*)
300 and found that there was significant overlap between the events detected through Bayesian and
301 model-congruence techniques ($p < 0.01$, Fisher's exact test). These events overlapped significantly
302 with replay events detected using traditional Bayesian decoding (*Figure 6–Figure Supplement 3*).
303 Thus, an HMM of the activity during population bursts captures the structure of neural activity in
304 two dimensional environments during complex tasks and can be used to decode events consistent
305 with trajectories through that environment.

Extra-spatial Information

307 As described earlier, while we observed a similar fraction of events to be similar by HMM-congruence
308 and Bayesian decoding, there was not an exact event-to-event correspondence. An intriguing po-
309 tential explanation is that the latent space represented in PBE sequential firing and captured by the
310 HMM is richer than simply the spatial structure of the present environment. In most hippocampal
311 ensemble recording experiments, maze or open field tasks are structured to intentionally map
312 memory elements to spatial behavior, and thus this potential richness is difficult to test. We used
313 two sample datasets to explore the potential of the HMM to capture extra-spatial richness in the
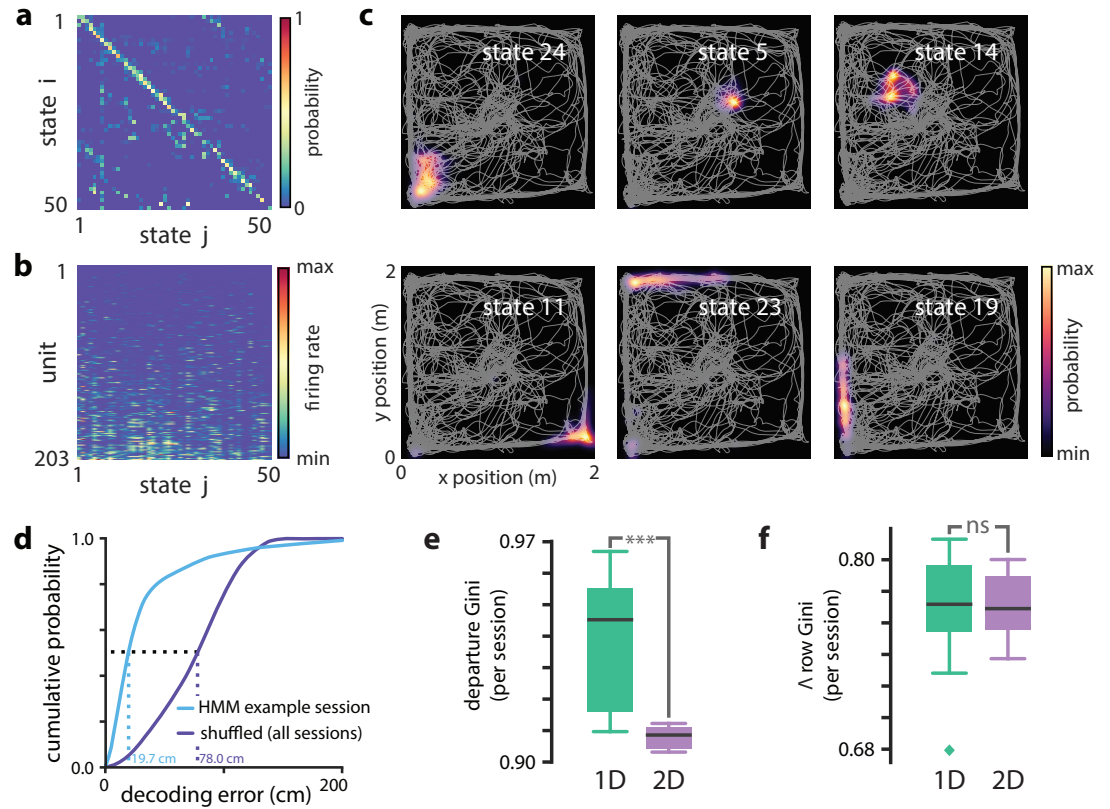
Figure 6. Modeling PBEs in open field. **a.** The transition matrix estimated from activity detected during PBEs in an example session in the open field. **b.** The corresponding observation model (203 neurons) shows sparsity similar to the linear track. **c.** Example latent state place fields show spatially-limited elevated activity in two dimensions. **d.** For an example session, position decoding through the latent space gives significantly better accuracy than decoding using the shuffled latent state place fields. **e.** Comparing the sparsity of the transition matrices (mean Gini coefficient of the departure probabilities) between the linear track and open field reveals that, as expected, over the sessions we observed, the open field is significantly *less sparse* ($p < 0.001$), since the environment is less constrained. **f.** In contrast, there is not a significant difference between the sparsity of the observation model (mean Gini coefficient of the rows) between the linear track and the open field. Note that the linear track models are sparser than in *Figure 2* due to using 50 states rather than 30 to match the open field.

Figure 6–Figure supplement 1. Open field PBE model states typically only transition to a few other states.

Figure 6–Figure supplement 2. Each neuron is active in only a few model states in the open field.

Figure 6–Figure supplement 3. lsPFs and position decoding in an open field.

Figure 6–Figure supplement 4. Examples of open field PBEs.

PBE sequences.

First, we considered the possibility that in the awake behaving animal, PBE activity might be sequential reactivation of environments other than the one being explored ("remote replay"). We reasoned that we could enhance the model's representation of remote environments by filtering out local replay from the training data. We evaluated how the model-quality of our HMM changed as progressively more sequences labeled as replay by Bayesian decoding were removed from the training data. In the linear track sessions we considered, we found that refining the training data resulted in models that lowered in quality at different rates as the threshold for Bayesian replay was decreased (*Figure 7*). Most, but not all, models dropped precipitously in quality: > 50% when we removed events detected as Bayesian replay at a 95% threshold, as would be expected if the HMM represented only the local environment. In many outlier sessions in which model quality decreased more slowly, the initial (baseline) model quality was low. Intriguingly, however, in at least one outlier session where model quality decreased slowly with refinement (blue line,*Figure 7*a), the initial model quality was still high, and we further noted that position decoding using lsPFs yielded relatively high error (blue dot, *Figure 7*b). Thus, we wondered whether this and similar sessions might have contained non-local or extra-spatial PBEs that were captured by the HMM.

In order to validate the concept of model-training refinement, we considered a dataset in which multiple environments were explored on the same day and remote replay was previously observed (*Karlsson et al., 2015*). These data consisted of a series of short exploratory sessions in which an animal first explored a novel maze (E1) and then was placed in a familiar one (E2). We identified awake PBEs during the familiar E2 session and used them to train an HMM. When we refined this model by removing Bayesian-significant local replay events from the training data, we found that the model quality decreased comparatively slowly (*Figure 7*a, green line), indicating that the HMM was capturing more than the local spatial structure. In contrast, when we used place fields from E1 to identify Bayesian-significant remote replay events and removed these from the training data, we found that the model quality decreased rapidly as with the general linear track cases (*Figure 7*a, red line). When we examined individual events in detail in this data, we found many examples in which HMM-significant, Bayesian non-significant PBEs decoded to extended state sequences which turned out to correspond to reactivation of the remote track (two are shown in *Figure 7*c–l). If we imagine that in this experiment data were only recorded during exploration of the familiar environment, classical Bayesian decoding would treat these events as noise, as shown in the bottom half of the two examples. In contrast, our HMM-based analysis finds these events to be significant, as shown in the top half of the two examples. Thus, by combining classical Bayesian decoding and HMM-congruence, we are able to identify a signature of when a HMM trained on PBEs captures sequential structure distinct from that dictated by the local environment. Additionally, in these cases, we show that specific non-local reactivation events can be identified.
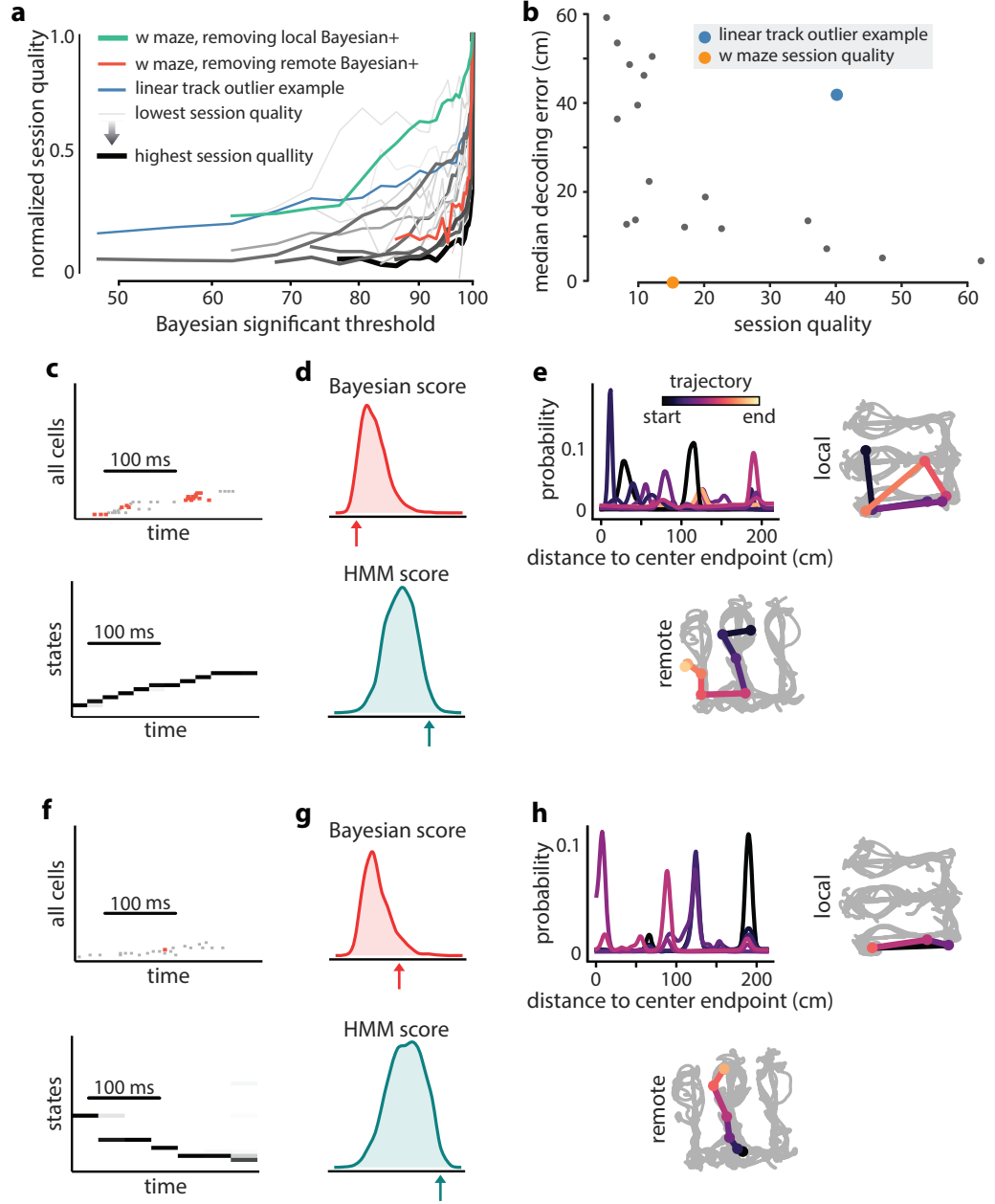
Figure 7. Examples of remote replay events identified with HMM-congruence. We trained and evaluated HMMs on the events that were not Bayesian significant (residual events) to identify potential extra-spatial structure. **a.** The normalized session quality drops as local-replay events above the Bayesian significance threshold are removed from the data. Each trace corresponds to one of the 18 linear track sessions, with the stroke width and the stroke intensity proportional to the baseline (all-events) session quality. The blue line identifies a session in which model quality drops more slowly, indicating the potential presence of extra-spatial information. The reduction in session quality for a W maze experiment with known extra-spatial information is even slower (green). When, instead, Bayesian-significant *remote* events are removed, rapid reduction in session quality is again revealed (red). **b.** The lsPF-based median decoding errors are shown as a function of baseline session quality for all 18 linear track sessions. The blue dot indicates the outlier session from panel **a** with potential extra-spatial information: this session shows high decoding error combined with high session quality. Session quality of the W maze session is also indicated on the x-axis (decoding error is not directly comparable). **c–n.** Two example HMM-congruent but not Bayesian-significant events from the W maze session are depicted to highlight the fact that congruence can correspond to remote replay. **c.** Spikes during ripple with local place cells highlighted (top panel) and the corresponding latent state probabilities (bottom panel) decoded using the HMM show sequential structure (grayscale intensity corresponds to probability). **d.** In this event, the Bayesian score relative to the shuffle distribution (top panel) indicates that the event is not-significant, whereas the HMM score relative to shuffles indicates (bottom panel) the ripple event is HMM-congruent. **e**. Estimates of position using local place fields show jumpy, multi-modal *a posteriori* distributions over space in 1D (top left panel) and 2D (top right panel; distribution modes and time is denoted in color). Bayesian decoding using the remote environment place fields (bottom panel) indicates that the sample event is a remote replay. Note that in a typical experiment, only the local place fields would be available. **f–h.** Same as **c–e**, but for a different ripple event.

350

351
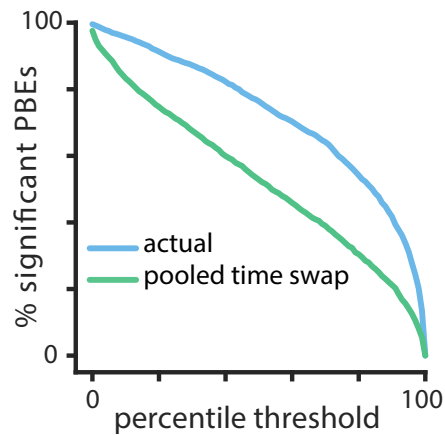
Figure 8. Temporal structure during a sleep period following object-location memory task. Using cross validation, we calculate the HMM-congruence score (which ranges from 0 to 1) for test PBEs. For each event, we also calculate the score of a surrogate chosen using a pooled time-swap shuffle across all test events. The distribution of scores of actual events is significantly higher than that of the surrogate data ($p < 0.001$, Mann–Whitney U test).

Finally, we considered the potential of our methodology for uncovering temporal patterns in PBE activity under scenarios where complex behavior does not permit identification of well-defined place-fields or in the absence of behavior, such as during sleep. As we have emphasized, a remarkable aspect of learning HMMs from PBE activity is that the model can be built entirely without behavioral data, so can our model capture significant sequential information outside of immobility periods during quiet waking? To demonstrate this potential, we examined HMMs trained on PBEs in sleep following the learning phase of an object-location memory task when animals explored three objects in an open field (see Material and Methods). Previous studies have demonstrated that subsequent recall of this memory is hippocampus-dependent, and requires consolidation in post-task sleep *Prince et al.* (*2014*); *Inostroza et al.* (*2013*). However, while this task involves spatial exploration of objects in an arena, whether the subsequent post-task sleep contains sequential structure and whether object memory is contained in this code has remained elusive (*Larkin et al., 2014*). In order to assess the presence of sequential structure in the PBEs, we first used cross validation to generate a distribution of sequence HMM-congruence scores. For each set of test PBEs, we also generated surrogates by shuffling time bins across events (pooled time-swap). Using our HMM-congruence score which explicitly tests for sequences through state space, the large difference between actual and shuffled score distributions indicates evidence for significant sequential structure in the PBEs ($p < 0.001$, Mann–Whitney U test, *Figure 8*). While more work is needed to evaluate the mnemonic relevance of these HMM-congruent sequences, these data support the notion that the HMM can uncover sequential activity in sleep away from the task environment. This approach further demonstrates the utility of the HMM approach as an initial analysis of a novel dataset, or as a way of comparing the sequential content encoded in PBEs during different periods.

Discussion

Increasing lines of evidence point to the importance of hippocampal ensemble activity during PBEs in guiding on-going behavior and active learning. Despite being the strongest output patterns of the hippocampus, however, this activity has been assumed to be interpretable only in the context of other theta-associated place cell activity expressed during behavior. Our findings demonstrate that over the course of a behavioral session, ensemble activity during PBEs alone is sufficient to form a model which captures the spatial relationships within an environment. This suggests that areas downstream of the hippocampus might be able to make use solely of PBE activity to form

models of external space. In an extreme view, place cell activity might merely subserve the internal mechanisms in the hippocampus which generate PBE sequences. To the extent that animals might wish to use the spatial code obtained from PBEs to identify their current location, we show that this can be done after translating ensemble activity into the latent states of the model. Do the PBEs contain "full information" about the environment? Bayesian decoding of location from place cell activity results in lower error than location estimates generated using the latent states and lsPFs. This suggests that the manifold defined by the HMM may not capture all the dimensions of information represented during exploration. However, it is possible that with more PBE data, we would learn a more refined state space. Thus, the difference between the latent space represented during behavior and within PBEs may be an interesting focus of future study.

When we examined the transition matrices we learned from PBEs, we found that they were marked by significant sparsity. This sparsity results from the sequential patterns generated during PBEs. Latent variable models have previously been used to analyze the structure of hippocampal place cell activity (*Chen et al., 2012*, *2014*; *Dabaghian et al., 2014*). In these studies, the learned transition matrices were mapped to undirected graphs which could be analyzed using topological measures. It is intriguing that similar structure is apparent in PBE activity. For example, we observed that transition matrices learned from PBEs associated with linear track behavior were significantly sparser than those learned from the open field, which we hypothesize is a consequence of the greater freedom of behavior in the latter (a topological difference). Whether hippocampal PBE activity must always be sequential, i.e., evolve through a sparsely-connected latent space, is an open and interesting question, as are differences between the latent state space dynamics learned during PBEs and those learned from place cell activity.

Graded, Non-binary Replay Detection

Remarkably, evaluating the congruence or likelihood of test data against our HMM provided a highly novel method to detect events that are consistent with replay, without a need to access the "play" itself. In the process of evaluating the potential of HMMs for detecting replay, we developed an approach to compare different replay-detection strategies. Our results highlight how the data does not readily admit to a strict separation between "replay" and "non-replay" events. While it is possible that with additional shuffles or other restrictions (*Silva et al., 2015*), automated performance might be rendered closer to human-labeling, even human scorers had variation in their opinions. This calls into doubt judgments of memory-related functions which build on a binary distinction between replay and non-replay sequences. Model congruence, either as a raw statistical likelihood or weighted against a shuffle distribution, seems to be a very reasonable metric to associate with individual PBEs. Moreover, evaluating congruence with an HMM does not require access to repeated behavioral sequences, which may be infeasible under widely-used single- or few-trial learning paradigms or when the events involve replay of a remote internalized environment. Given these benefits, along with computational efficiency, we would suggest that future analyses of the downstream impact of hippocampal reactivation regress effects against this measure rather than assuming a binary distinction.

Learning, Model Congruence and Replay Quality

Not surprisingly, the rate of PBEs had a large effect on our ability to measure model congruence. Interestingly, it has been noted that the density of PBEs is higher during early exposure to a novel environment (*Cheng and Frank, 2011*; *Frank et al., 2004*; *Kemere et al., 2013*; *Kudrimoti et al., 1999*). This might suggest that for the animal, PBE activity could be an important source for generating models of the world when the animal is actively learning about the environment. If as hypothesized, replay is a form of rehearsal signal generated by the hippocampus to train neocortical modules (*McClelland et al., 1995*; *Buzsáki, 1989*), then indeed the brain's internal machinery may also be evaluating whether a given sequential PBE pattern is congruent and consistent with previously observed PBEs. In later sessions, as animals have been repeatedly

exposed to the same environments, downstream regions will have already witnessed many PBEs from which to estimate the structure of the world. Overall, our approach provides a novel viewpoint from the perspective of hippocampal PBEs. An interesting future line of inquiry would be to assess the extent to which a model built on PBEs during first experience of a novel environment is slower or faster to converge to the final spatial map than models built on theta-associated place activity.

Application to Extra-spatial Behaviors

We have analyzed data gathered in experiments in which rats carried out simple spatial navigation tasks. Thus, to some extent it is not surprising that when we decoded ensemble activity during behavior we found that spatial positions the animal is exploring are strongly associated with the latent states.

We anticipate that our approach for calculating lsPFs would be equally useful in tasks in which the hippocampal map is organized around time (*Eichenbaum, 2014*; *Rodriguez and Levy, 2001*) or other continuous variables (e.g. sound frequency (*Aronov et al., 2017*)). Our two proof-of-concept analyses, however, suggest that it should be possible to use HMMs to infer the presence of extra-spatial sequential reactivation in PBEs. For example, we showed that there is significant sequential structure during sleep after an animal explores novel objects in an environment. We anticipate that careful experimental design and further algorithmic development would allow for the conjunctive coding of object identity and spatial locations to be detected in the latent states we learn from PBEs, with model-congruence providing a tool to study sequential hippocampal reactivation in these types of tasks.

Conjunctive, non-spatial information might be one source of the apparent variability that results in many PBEs not being detected as replay using traditional Bayesian decoding. Another proposed source of this variability is reactivation of other environments. Our second proof-of-concept analysis suggests that HMMs learned from PBEs can, in fact, capture the spatial structure of environments beyond the one the animal is currently exploring. It appears that it should be possible to use only the PBEs and information about the place-cell map of the local environment to refine the training set for remote replay activity and learn the structure of a remote environment. While we used Bayesian decoding to detect putative local replays, we anticipate related approaches might use an HMM or other approaches to model local place cell activity.

Future possibilities

It has been previously observed that the rate of hippocampal reactivations in PBEs during awake behavior is much higher than during sleep (*Grosmark and Buzsáki, 2016*; *Karlsson and Frank, 2008*), but the reasons for this are not well understood. One hypothesis is that many sleep PBEs contain the reactivation of contexts other than those measured during a behavioral experiment. Another hypothesis is that sleep activity involves remodeling of dynamic network architectures (*Buhry et al., 2011*; *Tononi and Cirelli, 2014*). Our approach has the potential to illuminate some sources of variability during sleep. While we have given preliminary evidence that information about a remote context can be present in PBEs along with the local context, further work is required to understand how our model's ability to capture this structure scales with the number of different contexts. With sufficient data, our HMM approach should be able to learn disjoint sets of latent states (or "sub-models") which would capture these separate contexts and allow us to test this possibility. Alternatively, sleep PBEs could yield models which represent a known behavioral context but are markedly different (e.g., less sparse) than those learned from awake PBEs. This might support the network remodeling function of sleep. In the latter case, we might imagine that only a small subset of sleep PBEs—corresponding to learning-related replay—would be congruent with a model learned from awake PBE data.

Conclusions

We have demonstrated a new analytical framework for studying hippocampal ensemble activity which enables primacy of PBEs in model formation. We use an unsupervised learning technique commonly used in the machine learning field to study sequential patterns, the hidden Markov model. This contrasts with existing approaches in which the model—estimated place fields for the ensemble—is formed using the theta-associated place cell activity. We find that our PBE-first approach results in a model which still captures the spatial structure of the behavioral tasks we studied. Additionally, we demonstrate that we can use model-congruence as a tool for assessing whether individual PBEs contain hippocampal replay. Finally, we present proofs-of-concept that this analytical approach can detect the presence of sequential reactivation in experimental scenarios in which existing approaches are insufficient. Thus, the use of unsupervised learning of latent variable models—specifically HMMs and statistical congruence as a marker of individual events—bears much promise for expanding our ability to understand how PBEs enable the cognitive functions of the hippocampus.

Materials and Methods

Experiment paradigm/Neural data recording

We analyzed neural activity recorded from the hippocampus of rats during periods in which they performed behavioral tasks in different paradigms. First, we considered data from animals running back and forth in a linear track 150 or 200 cm long. As previously reported using these same data (*Diba and Buzsáki, 2007*), we recorded neural activity using chronically-implanted silicon probes to acquire the activity of hippocampal CA1/CA3 neurons. From these experiments, we chose sessions during which we observed at least 20 place cells during active place-field exploration, and at least 30 PBEs (see below). Place cells were identified as pyramidal cells which had (i) a minimum peak firing rate of 2 Hz, (ii) a maximum mean firing rate of 5 Hz, and (iii) a peak-to-mean firing rate ratio of at least 3, all estimated exclusively during periods of run (as defined before, that is, when the animal was running > 10 cm/s). This selection yielded $n = 18$ session with 41–203 neurons (36–186 pyramidal cells). All procedures were approved by the Institutional Animal Care and Use Committee of Rutgers University and followed US National Institutes of Health animal use guidelines (protocol 90-042).

A second dataset used tetrodes to record a large number (101–242) of putative pyramidal neurons in area CA1 during two sessions each in four rats. Briefly, as was previously reported using these data (*Pfeiffer and Foster, 2013*, *2015*), rats explored an arena in which there were 36 reward sites. In each session, one site was designated as "home". During a session, rats would repeatedly alternate between retrieving a random reward site in one of the remaining 35 locations and retrieving a reward at the home location. All procedures were approved by the Johns Hopkins University Animal Care and Use Committee and followed US National Institutes of Health animal use guidelines (protocols RA08M138, RA11M16, and RA14M48).

In order to investigate remote replay, we used data from an experiment in which this phenomenon has been previously reported (*Karlsson and Frank, 2009*). Briefly, rats were implanted with multi-electrode microdrives with tetrodes targeting CA1 and CA3. They were trained to carry out a continuous-alternation task in an initially novel "w"-shaped maze (E2) for liquid reward for multiple daily run sessions interspersed by rest-periods in an enclosed box. After they learned the task, they were introduced to a novel w-maze (E1) in a different orientation in which they had two run sessions followed by a run in the now-familiar E2. For our proof-of-concept analysis (*Figure 7*), we used data from the second day of the novel maze (i.e., third and fourth exposures) in animal 'Bon'.

Finally, we recorded neural activity during an object-location memory task using a 32-channel silicon probes (Buzsaki32, Neuronexus, MI) equipped with light fibers lowered to area CA1 of the dorsal hippocampus. The animal was previously infused with AAV-CamKIIa-ArchT-GFP for the

527 purpose of another experiment. Putative pyramidal cells and interneurons were distinguished
528 based on their spike waveforms and spike auto-correlograms. On the day before the recordings,
529 the animal was repeatedly exposed to an empty test chamber on four successive six minute blocks,
530 interleaved by three minute rest periods in the home cage. On the recording day, the first of these
531 six-minute blocks was again the empty test chamber, but on the remaining blocks, the animal was
532 exposed to a fixed configuration of three different novel objects placed in the northeast, center
533 and southeast corners of the box. These blocks were again interleaved with three minute rest
534 periods in the home cage. The test chamber was a 60×60 cm^2 box with a local cue (8.5 in. $\times$
535 11 in. sheet printout) placed on one test wall. Following the last acquisition exposure, the animal
536 was returned to its home cage for a four hour extended sleep period. The subsequent day, one
537 of the objects in the box was displaced and the animal was reintroduced into the box to test for
538 interactions with the displaced versus non-displaced objects. All procedures were approved by
539 the Institutional Animal Care and Use Committee of the University of Wisconsin-Milwaukee and
540 followed US National Institutes of Health animal use guidelines (protocol 13-14 #28)

Population burst events

542 To identify PBEs in the linear track data, a spike density function (SDF) was calculated by counting
543 the total number of spikes across all recorded single and multi-units in non-overlapping 1 ms
544 time bins. The SDF was then smoothed using a Gaussian kernel (20 ms standard deviation, 60 ms
545 half-width). Candidate events were identified as time windows with a peak SDF of at least three
546 standard deviations above the mean calculated over all the session. The boundaries of each event
547 were set to time points of crossing the mean, preceding and following the peak. Events during
548 which animals were moving (average movement speed of > 5 cm/s) were excluded from all further
549 analyses to prevent possible theta sequences from biasing our results. For analysis, we then binned
550 each PBE into 20 ms (non-sliding) time bins. Spikes from putative interneurons (mean firing rate
551 when moving > 10 Hz) were excluded, as were events with duration less than four time bins or with
552 fewer than four active pyramidal cells. For the open field data, we used the previously reported
553 criteria (*Pfeiffer and Foster, 2013*) for identifying PBEs prior to binning (10 ms standard deviation
554 kernel, minimum of 10% of units active, duration between 50 ms and 2000 ms).

Hidden Markov model of PBE activity

556 We trained HMMs on the PBEs. In an HMM, an unobserved discrete latent state q_t evolves through
557 time according to a first order Markov process. The temporal evolution of the latent state is
558 described by the $M \times M$ matrix $\mathbf{A}$, whose elements $\{a_{ij}\}$ signify the probability after each time
559 bin of transitioning from state i to state j, $a_{ij} = \Pr\left(q_{t+1} = j | q_t = i\right)$. The number of states, M, is a
560 specified hyperparameter. We found that our results were insensitive to the value of M through a
561 wide range of values from 20 to 100 (*Figure 3–Figure Supplement 1*). During each time bin of an
562 event, the identity of the latent state influences what is observed via a state-dependent probability
563 distribution. We modeled the N-dimensional vector of binned spiking from our ensemble of N
564 neurons at time t, O_t, as a Poisson process. Specifically, for each state, i, we model neuron n as
565 independently firing according to a Poisson process with rate λ_{ni}.

$$\Pr\left(O_t | q_t = i\right) = \prod_{n=1}^{N} \Pr(o_{nt} | q_t = i) \propto \prod_{n=1}^{N} (\lambda_{ni})^{o_n} \exp\left(-\lambda_{ni}\right)$$

566 where o_{nt} is the number of spikes observed from neuron n at time t. The final parameter which
567 specifies our model is the probability. distribution of the initial state for a given event, $\pi_i = Pr(q_1 = i)$.
568 Thus, our model is specified by parameters $\theta = \{\mathbf{A}, \mathbf{\Lambda}, \boldsymbol{\pi}\}$, where $\mathbf{\Lambda} = \{\lambda_{ni}S\}$ is an $N \times M$ matrix and
569 $\boldsymbol{\pi} = \{\pi_i\}$ is an N-dimensional vector.
570   To learn model parameters, we follow the well-known iterative EM procedure (*Rabiner, 1989*),
571 treating each training PBE as an observation sequence. In order to regularize the model, we impose
572 a minimum firing rate for each neuron of 0.001 (0.05 Hz) during the M-step of EM. For a given PBE

573 (i.e., observation sequence) with K bins, we use the "forward-backward algorithm" (**Rabiner, 1989**)
574 to calculate the probability distribution of the latent state for each time bin, $\Pr(q_t|O_1, \dots, O_t, \dots, O_K)$.
575 For a particular time bin, t, in a given sequence, the forward-backward algorithm allows information
576 from all observation bins, previous and subsequent, to affect this state probability distribution
577 (as well the observation bin at time t). The forward-backward algorithm also efficiently calculates
578 the "score", or likelihood of the complete sequence, $\Pr(O_1, \dots, O_K)$. All HMMs learned in this work
579 used five-fold cross validation, i.e., the PBEs were divided into five randomly selected fifths ("folds"),
580 and then each fold was evaluated as a test set, with the model trained using the remaining four
581 folds. We define the model likelihood of an HMM as the product of the scores of each event using
582 this five-fold cross validation. To initially evaluate model learning, we compared model likelihoods
583 calculated using real and shuffled test data. Models which have learned to properly represent the
584 data should show significant increases. To quantify the presence of PBE sequences in a model we
585 used a model quality metric as described below.

Ordering states for visualization

587 For visualization, we wanted to order the states to maximize the super diagonal of the transition
588 matrix. We used a greedy approach which typically yields this solution. We started by assigning
589 the first index to the state with the highest initial probability and added states based on the most
590 probable state transitions. The undirected connectivity graphs were then generated from this
591 transition matrix, averaging the strength of reciprocal connections, a_{ij} and a_{ji}.

Surrogate datasets and shuffle methods

593 In order to analyze the HMMs we learned, we compared them against different types of surrogate
594 datasets obtained by shuffling the neural activity during PBEs in distinct ways. 1) **Temporal shuffle**:
595 within each event, the binned spiking activity was circularly permuted across time for each unit,
596 independently of other units. This goal of this shuffle is to disrupt unit co-activation, while maintain-
597 ing the temporal dynamics for each unit. 2) **Time-swap shuffle**: within each event, the order of the
598 binned columns of neural activity was randomly permuted across time, coherently across units. The
599 goal of this shuffle is to change the temporal dynamics of ensemble activity, while maintaining unit
600 co-activation. 3) **Poisson surrogate "shuffle"**: we estimated each unit's mean firing rate across all
601 PBEs, and then produced surrogate PBEs from independent Poisson simulations according to each
602 unit's mean firing rate. 4) **Pooled time-swap shuffle**: the order of the binned columns of neural
603 activity was randomly permuted across all pooled events, coherently across units. This shuffle has
604 been previously used in Bayesian replay detection (**Davidson et al., 2009**).

Calculating sparsity and connectivity of the model parameters

606 Sparsity of the transitions from individual states (departure sparsity) was measured by calculating
607 the Gini coefficient of corresponding rows of the transition matrix (**Hurley and Rickard, 2009**). The
608 Gini coefficient is a measure of how variable the values of this probability distribution are, with
609 equality across states corresponding to a coefficient of zero (minimal sparsity), and a singular
610 distribution with a probability-one transition to a single other state corresponding to a coefficient
611 of one (maximal sparsity). The sparsity of the full transition matrix was calculated by averaging
612 the Gini coefficient across rows. For analyses of PBE models from linear tracks, we computed the
613 mean sparsity across states for each of the 250 surrogate datasets, and these means were used to
614 generate the box plots of *Figure 2*c. Note that for the actual data, we generate a distribution by
615 randomly initializing the model 250 times and calculating the mean sparsity over all initializations.
616 For analyses of models learned from PBEs in open fields (and the linear track comparison with
617 50 states), we created 50 surrogates/random initializations (*Figure 6–Figure Supplement 1*). To
618 compare across sessions, we calculated the mean sparsity by averaging over all 250 surrogate
619 datasets to obtain a single mean sparsity per session, so that $n = 18$ per-session means were used
620 to create the box-plots of *Figure 2*e.

⁶²¹ Firing rates can be highly variable for different units. Thus, when evaluating the sparsity of
⁶²² the observation matrix, we measured the extent to which individual units were specifically active
⁶²³ in a few states by calculating the Gini coefficients of the rows of the observation matrix. As with
⁶²⁴ transitions, we calculated mean sparsity across units for each surrogate dataset (e.g., linear track,
⁶²⁵ *Figure 2*d; open field, *Figure 6–Figure Supplement 2*), and we then averaged over all surrogate
⁶²⁶ datasets to obtain a per-session average, used in *Figure 2*f.

Model connectivity and sequences

⁶²⁸ To measure the degree of sequential connectivity within the graph corresponding to the transition
⁶²⁹ matrix—with nodes and edges representing the states and transitions, respectively—we developed
⁶³⁰ an algorithm for measuring the length of the longest path that can be taken through the graph. This
⁶³¹ method is analogous to the "depth-first search" algorithm for traversing the graph's tree structure
⁶³² without backtracking. First, we made an adjacency matrix for a corresponding unweighted directed
⁶³³ graph by binarizing the transition matrix using a threshold of 0.2 on the transition probabilities.
⁶³⁴ Starting from each node, we then found the longest path that ended at either a previously visited
⁶³⁵ node or a terminal node (a node without any outgoing edges). To compare models trained on actual
⁶³⁶ versus surrogate datasets, we adjusted the thresholds to match the average degree (defined as the
⁶³⁷ average number of edges per node) between the models, thus ruling out possible effects due to
⁶³⁸ differences in the number of graph edges. We carried out this analysis on the same set of models
⁶³⁹ that were generated for analyzing sparsity. To compare across sessions, we calculated the median
⁶⁴⁰ maximum path length for each session ($n = 18$) and used the per-session medians to generate box
⁶⁴¹ plots of *Figure 2–Figure Supplement 3*c.

Latent state place fields

⁶⁴³ To calculate the latent state place fields, we first identified bouts of running by identifying periods
⁶⁴⁴ when animals were running (speed > 10 cm/s). We then binned the spiking during each of these
⁶⁴⁵ bouts in 100 ms bins. Using the forward-backward algorithm *Rabiner* (*1989*) and the HMM model
⁶⁴⁶ parameters learned from PBEs, we decoded each bout into a sequence of latent state probability
⁶⁴⁷ distributions, $Pr(q_t|O_t)$. Using the track positions corresponding to each time bin, we then found the
⁶⁴⁸ average state distribution for each position bin, x_p, and normalized to yield a distribution for each
⁶⁴⁹ state, $Pr(x_p|q_t = i)$.

Decoding position from latent state sequences

⁶⁵¹ We used the lsPFs to decode the animal's position after determining the probability of different
⁶⁵² latent state trajectories during bouts of running. With five-fold cross validation, we estimated lsPFs
⁶⁵³ in a training dataset, then used the HMM model to decode latent state trajectory distributions from
⁶⁵⁴ ensemble neural activity in the test data. The product of lsPFs and decoded latent state distribution
⁶⁵⁵ at time t is the joint distribution $Pr(x_p, q_t|O_t)$. We decode position as the mean of the marginal
⁶⁵⁶ distribution $Pr(x_p|O_t)$.

Bayesian Replay Detection

⁶⁵⁸ We followed a frequently used Bayesian decoding approach to detect replay in our 1D data (*Kloost-*
⁶⁵⁹ *erman, 2012*). For each 20 ms time bin t within a PBE, given a vector comprised of spike counts
⁶⁶⁰ from N units, $O_t = (o_{1t}\ o_{2t}\ \dots\ o_{Nt})$ in that bin, the posterior probability distribution over the binned
⁶⁶¹ track positions was calculated using Bayes' rule:

$$Pr\left(x_p|O_t\right) = \frac{Pr(O_t|x_p)Pr(x_p)}{\sum_{q=1}^{P} Pr(O_t|x_q)Pr(x_q)},$$

662 where x_p is the center of p-th linearized position bin (of P total bins). We assumed Poisson firing
663 statistics, thus the prior probability, $\Pr(O_t|x_p,)$, for the firing of each unit n is equal to

$$Pr\left(O_t|x_p\right) = \prod_{n=1}^{N} \Pr\left(o_{nt}|x_p,\right) \propto \prod_{n=1}^{N} (\tau\lambda_{np})^{o_{nt}} \exp\left(-\tau\lambda_{(n,p)}\right)$$

664 where τ is the duration of time bin (100 ms during estimation, 20 ms during decoding), and λ_{np}
665 characterizes the mean firing rate of the n-th unit in the p-th position bin. We assumed a uniform
666 prior distribution $Pr(x_p)$ over the position bins.
667   For each PBE, the estimated posterior probability distribution was used to detect replay as
668 follows. Many (35,000) lines with different slopes and intercepts were sampled randomly following
669 the approach in (*Kloosterman, 2012*). The Bayesian replay score for a given event was the maximum
670 score obtained from all candidate lines, where the score for a particular line was defined as the
671 mean probability mass under the line, within a bandwidth (of 3 cm). For time bins during which the
672 sampled line fell outside of the extent of the track, the median probability mass of the corresponding
673 time bin was used, and for time bins during which no spikes were observed, we used the median
674 probability mass across all on-track time bins. To evaluate the significance of this score, for each
675 event we generated 5,000 surrogates of the posterior probability distribution by cycling the columns
676 (i.e., for each time bin, circularly permuting the distribution over positions by a random amount)
677 and calculated the replay score for each surrogate. The Monte Carlo p-value for each event was
678 obtained from the number of shuffled events with replay scores higher than the raw data. The
679 threshold for significance was varied as described in the text. For the open field, we used previously
680 reported criteria (*Pfeiffer and Foster, 2013*) to identify replay events from PBEs.

Replay detection via PBE model congruence

682 To identify replay as model congruence, for each PBE, we used the forward-backward algorithm to
683 calculate the sequence likelihood $\Pr(O_1, \ldots, O_K)$, as defined earlier. Using five-fold cross validation,
684 the parameters of a HMM were learned from training PBEs. The sequence score was then calculated
685 for each event in the test data. To evaluate the significance of this score, for each event we generated
686 5,000 surrogate scores using a computationally-efficient scheme. Specifically, for each surrogate,
687 we randomly shuffle the rows of the transition matrix, excepting the diagonal. By maintaining the
688 diagonal (i.e., transitions that begin and end in the same state) and leaving the observation model
689 unchanged, this shuffle specifically selects against PBEs in which the latent states do not evolve
690 in temporal sequences. The Monte Carlo p-value for each event was calculated as the fraction of
691 shuffled events with HMM sequence scores higher than the raw data. The threshold for significance
692 was varied as described in the text. Note that while we describe this as HMM-congruence, we
693 have maintained the diagonal of the transition matrix, which specifically selects against PBEs
694 which might be model-congruent by maintaining a single state over many time bins. In reality
695 there are other dimensions of the HMM that we could assess congruence against, for example
696 the observation model, the initial state distribution, or combinations of these and the transition
697 matrix. In comparing against Bayesian decoding, our current definition seemed most appropriate
698 for sequence detection, but we can imagine future studies expanding on our approach.

Human scoring and detection comparison

700 We organized a group of human scorers to visually evaluate whether individual PBEs should
701 be described as replay. More specifically, scorers were only presented with Bayesian decoded
702 probability distributions such as those in *Figure 4*a, but without access to the spike raster or any
703 additional information. The scorers included six graduate students (including one of the authors)
704 and two undergraduates, all of whom were generally familiar with the concept of hippocampal
705 replay. We built an automatic presentation system which would display each event in random order,
706 and record one of six possible scores: "excellent" (highly sequential with no jumps and covering
707 most of the track), "good" (highly sequential with few or no jumps), "flat" (decoded position stayed

mostly in the same place, i.e. no temporal dynamics), "uncertain" (some semblance of structure, but not enough to fall into any of the previous categories) or "noise" (no apparent structure, or nonsensical trajectories such as teleportation). An event was then designated as replay if it was labeled as "excellent" or "good" by a majority of scorers (ties were labeled as non-replay).

To calculate an ROC curve for replay detection algorithms, we used our shuffle statistics for each event to create a vector which related the significance threshold (e.g., 99%) to the label supplied by the algorithm (i.e., significant replay or not). Then, as a function of threshold, the sensitivity (fraction of true positives identified) and selectivity (fraction of true negatives identified) were averaged over events to yield an ROC curve. To evaluate whether the AUC differed between Bayesian and model-congruence techniques we used a bootstrap approach. To generate a null hypothesis, we combined the event/threshold vectors from both groups, and then sampled two random groups (A and B) with replacement from the pooled data. The AUCs for these two random groups of events were measured, and a distribution for the difference between the randomly chosen AUCs was calculated. The two-sided p-value we report is the fraction of differences in random AUCs which are more extreme than the actual difference.

HMM model quality across sessions

In order to understand the extent to which an HMM trained on PBEs from a given session contained sequentially-structured temporal dynamics, we calculated the "session quality" (equivalently model quality) as follows. Again using five-fold cross validation, we learn an HMM on the training subset of PBEs, and score (using the forward-backward algorithm, as before), the remaining subset of test PBEs. Then, we also score a pooled time-swap surrogate of the test PBEs and we repeat this pooled time-swap scoring $n = 2500$ times. Finally, we obtain a z score for each PBE by comparing the score from the actual test PBE, to the distribution of pooled time-swap scores of the corresponding PBE. The session quality is then defined as the average of these z scores, over all events in a session. This measure of session quality was then used to detect the presence of putative remote replay events or other extra-spatial structure in PBEs, since a high session quality after removing local Bayesian significant events is highly suggestive of remaining (unexplained) sequential structure.

Software and data analysis

Data analyses were performed using MATLAB and Python. Jupyter notebooks (using Python) are available at https://github.com/kemerelab/UncoveringTemporalStructureHippocampus, where most of the results presented here are reproduced. We have also developed and open-sourced a Python package (namely `nelpy`) to support the analyses of electrophysiology data with HMMs, which is available from https://github.com/nelpy (*Ackermann et al., 2018*).

Acknowledgments

References

Ackermann E, Chu J, Dutta S, Kemere C, Nelpy: neuroelectrophysiology object model and data analysis in Python; 2018. doi: 10.5281/zenodo.1219790. https://github.com/nelpy.

Aronov D, Nevers R, Tank DW. Mapping of a non-spatial dimension by the hippocampal–entorhinal circuit. Nature. 2017; 543(7647):719.

Buhry L, Azizi AH, Cheng S. Reactivation, replay, and preplay: how it might all fit together. Neural plasticity. 2011; 2011.

Buzsáki G. Hippocampal sharp waves: their origin and significance. Brain research. 1986; 398(2):242–252.

Buzsáki G. Two-stage model of memory trace formation: a role for "noisy" brain states. Neuroscience. 1989; 31(3):551–570.

Buzsáki G. Hippocampal sharp wave-ripple: A cognitive biomarker for episodic memory and planning. Hippocampus. 2015; 25(10):1073–1188.

Buzsáki G, Vanderwolf CH, et al. Cellular bases of hippocampal EEG in the behaving rat. Brain Research Reviews. 1983; 6(2):139–171.

Carr MF, Jadhav SP, Frank LM. Hippocampal replay in the awake state: a potential substrate for memory consolidation and retrieval. Nature neuroscience. 2011; 14(2):147–153.

Chen Z, Gomperts SN, Yamamoto J, Wilson MA. Neural representation of spatial topology in the rodent hippocampus. Neural computation. 2014; 26(1):1–39.

Chen Z, Kloosterman F, Brown EN, Wilson MA. Uncovering spatial topology represented by rat hippocampal population neuronal codes. Journal of computational neuroscience. 2012; 33(2):227–255.

Chen Z, Wilson MA. Deciphering Neural Codes of Memory during Sleep. Trends in Neurosciences. 2017; .

Cheng S, Frank LM. New experiences enhance coordinated neural activity in the hippocampus. Neuron. 2008; 57(2):303–313.

Cheng S, Frank LM. The structure of networks that produce the transformation from grid cells to place cells. Neuroscience. 2011; 197:293–306.

Chrobak JJ, Buzsáki G. High-frequency oscillations in the output networks of the hippocampal–entorhinal axis of the freely behaving rat. Journal of neuroscience. 1996; 16(9):3056–3066.

Dabaghian Y, Brandt VL, Frank LM. Reconceiving the hippocampal map as a topological template. Elife. 2014; 3:e03476.

Davidson TJ, Kloosterman F, Wilson MA. Hippocampal replay of extended experience. Neuron. 2009; 63(4):497–507.

Deppisch J, Pawelzik K, Geisel T. Uncovering the synchronization dynamics from correlated neuronal activity quantifies assembly formation. Biological cybernetics. 1994; 71(5):387–399.

Diba K, Buzsáki G. Forward and reverse hippocampal place-cell sequences during ripples. Nature neuroscience. 2007; 10(10):1241–1242.

Diekelmann S, Born J. The memory function of sleep. Nature Reviews Neuroscience. 2010; 11(2):114–126.

Dupret D, O'neill J, Pleydell-Bouverie B, Csicsvari J. The reorganization and reactivation of hippocampal maps predict spatial memory performance. Nature neuroscience. 2010; 13(8):995–1002.

Ego-Stengel V, Wilson MA. Disruption of ripple-associated hippocampal activity during rest impairs spatial learning in the rat. Hippocampus. 2010; 20(1):1–10.

Eichenbaum H. Time cells in the hippocampus: a new dimension for mapping memories. Nature Reviews Neuroscience. 2014; 15(11):732.

Foster DJ, Wilson MA. Reverse replay of behavioural sequences in hippocampal place cells during the awake state. Nature. 2006; 440(7084):680–683.

Frank LM, Stanley GB, Brown EN. Hippocampal plasticity across multiple days of exposure to novel environments. Journal of Neuroscience. 2004; 24(35):7681–7689.

Fruchterman TMJ, Reingold EM. Graph Drawing by Force-directed Placement. Software – Practice & Experience. 1991; 21(11):1129–1164.

Girardeau G, Benchenane K, Wiener SI, Buzsáki G, Zugaro MB. Selective suppression of hippocampal ripples impairs spatial memory. Nature neuroscience. 2009; 12(10):1222–1223.

Grosmark AD, Buzsáki G. Diversity in neural firing dynamics supports both rigid and learned hippocampal sequences. Science. 2016; 351(6280):1440–1443.

Gupta AS, van der Meer MA, Touretzky DS, Redish AD. Hippocampal replay is not a simple function of experience. Neuron. 2010; 65(5):695–705.

Hurley N, Rickard S. Comparing measures of sparsity. IEEE Transactions on Information Theory. 2009; 55(10):4723–4741.

Inostroza M, Binder S, Born J. Sleep-dependency of episodic-like memory consolidation in rats. Behavioural brain research. 2013; 237:15–22.

Jadhav SP, Kemere C, German PW, Frank LM. Awake hippocampal sharp-wave ripples support spatial memory. Science. 2012; 336(6087):1454–1458.

Karlsson MP, Carr MF, Frank LM, Simultaneous extracellular recordings from hippocampal areas CA1 and CA3 (or MEC and CA1) from rats performing an alternation task in two W-shapped tracks that are geometrically identically but visually distinct. CRCNS.org; 2015. doi: 10.6080/K0NK3BZJ. http://dx.doi.org/10.6080/K0NK3BZJ.

Karlsson MP, Frank LM. Network dynamics underlying the formation of sparse, informative representations in the hippocampus. Journal of Neuroscience. 2008; 28(52):14271–14281.

Karlsson MP, Frank LM. Awake replay of remote experiences in the hippocampus. Nature neuroscience. 2009; 12(7):913–918.

Kemere C, Carr MF, Karlsson MP, Frank LM. Rapid and continuous modulation of hippocampal network state during exploration of new places. PloS one. 2013; 8(9):e73114.

Kemere C, Santhanam G, Byron MY, Afshar A, Ryu SI, Meng TH, Shenoy KV. Detecting neural-state transitions using hidden Markov models for motor cortical prostheses. Journal of neurophysiology. 2008; .

Kloosterman F. Analysis of hippocampal memory replay using neural population decoding. Neuronal Network Analysis: Concepts and Experimental Approaches. 2012; p. 259–282.

Kudrimoti HS, Barnes CA, McNaughton BL. Reactivation of hippocampal cell assemblies: effects of behavioral state, experience, and EEG dynamics. Journal of Neuroscience. 1999; 19(10):4090–4101.

Larkin MC, Lykken C, Tye LD, Wickelgren JG, Frank LM. Hippocampal output area CA1 broadcasts a generalized novelty signal during an object-place recognition task. Hippocampus. 2014; 24(7):773–783.

Lee AK, Wilson MA. Memory of sequential experience in the hippocampus during slow wave sleep. Neuron. 2002; 36(6):1183–1194.

Logothetis NK, Eschenko O, Murayama Y, Augath M, Steudel T, Evrard H, Besserve M, Oeltermann A. Hippocampal-cortical interaction during periods of subcortical silence. Nature. 2012; 491(7425):547–553.

McClelland JL, McNaughton BL, O'reilly RC. Why there are complementary learning systems in the hippocampus and neocortex: insights from the successes and failures of connectionist models of learning and memory. Psychological review. 1995; 102(3):419.

Nádasdy Z, Hirase H, Czurkó A, Csicsvari J, Buzsáki G. Replay and time compression of recurring spike sequences in the hippocampus. Journal of Neuroscience. 1999; 19(21):9497–9507.

O'Keefe J. Place units in the hippocampus of the freely moving rat. Experimental neurology. 1976; 51(1):78–109.

Pfeiffer BE, Foster DJ. Hippocampal place-cell sequences depict future paths to remembered goals. Nature. 2013; 497(7447):74–79.

Pfeiffer BE, Foster DJ. Autoassociative dynamics in the generation of sequences of hippocampal place cells. Science. 2015; 349(6244):180–183.

Prince TM, Wimmer M, Choi J, Havekes R, Aton S, Abel T. Sleep deprivation during a specific 3-hour time window post-training impairs hippocampal synaptic plasticity and memory. Neurobiology of learning and memory. 2014; 109:122–130.

Rabiner LR. A tutorial on hidden Markov models and selected applications in speech recognition. Proceedings of the IEEE. 1989; 77(2):257–286.

Radons G, Becker J, Dülfer B, Krüger J. Analysis, classification, and coding of multielectrode spike trains with hidden Markov models. Biological cybernetics. 1994; 71(4):359–373.

Rodriguez P, Levy WB. A model of hippocampal activity in trace conditioning: Where's the trace? Behavioral Neuroscience. 2001; 115(6):1224.

844 **Siapas AG**, Wilson MA. Coordinated interactions between hippocampal ripples and cortical spindles during
845   slow-wave sleep. Neuron. 1998; 21(5):1123–1128.

846 **Silva D**, Feng T, Foster DJ. Trajectory events across hippocampal place cells require previous experience. Nature
847   neuroscience. 2015; 18(12):1772–1779.

848 **Tononi G**, Cirelli C. Sleep and the price of plasticity: from synaptic and cellular homeostasis to memory
849   consolidation and integration. Neuron. 2014; 81(1):12–34.

850 **Yamamoto J**, Tonegawa S. Direct Medial Entorhinal Cortex Input to Hippocampal CA1 Is Crucial for Extended
851   Quiet Awake Replay. Neuron. 2017; 96(1):217–227.
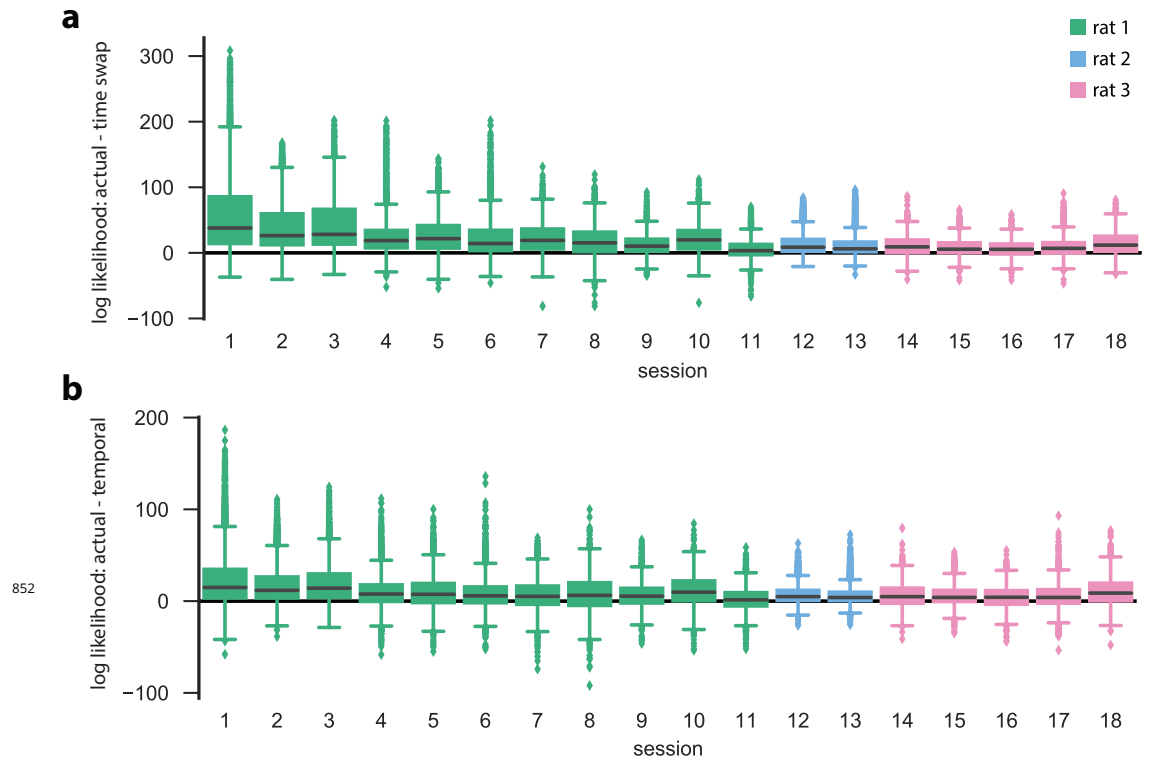
Figure 1–Figure supplement 1. Actual cross-validated test data and surrogate test data evaluated in actual-data-optimized HMMs for all 18 linear track sessions. For each session, we performed five-fold cross validation to score the validation (=test) set in an HMM that was learned on the corresponding training set. In addition, two surrogate datasets of the validation data (obtained by either temporal shuffle or time-swap shuffle) were scored in the same HMM as the actual validation data. $k = 50$ shuffles of each event and of each type were performed. **a.** Difference between the data log likelihoods of actual and time-swap surrogate test events, evaluated in the actual train-data-optimized models. **b.** Same as in **a.**, except that the differences between the actual data and the temporal surrogates are shown. For each of the $n = 18$ sessions, the actual test data had a significantly higher likelihood than either of the shuffled counterparts ($p < 0.001$, Wilcoxon signed-rank test). Sessions are arranged first by animal, and then by number of PBEs, in decreasing order.

852
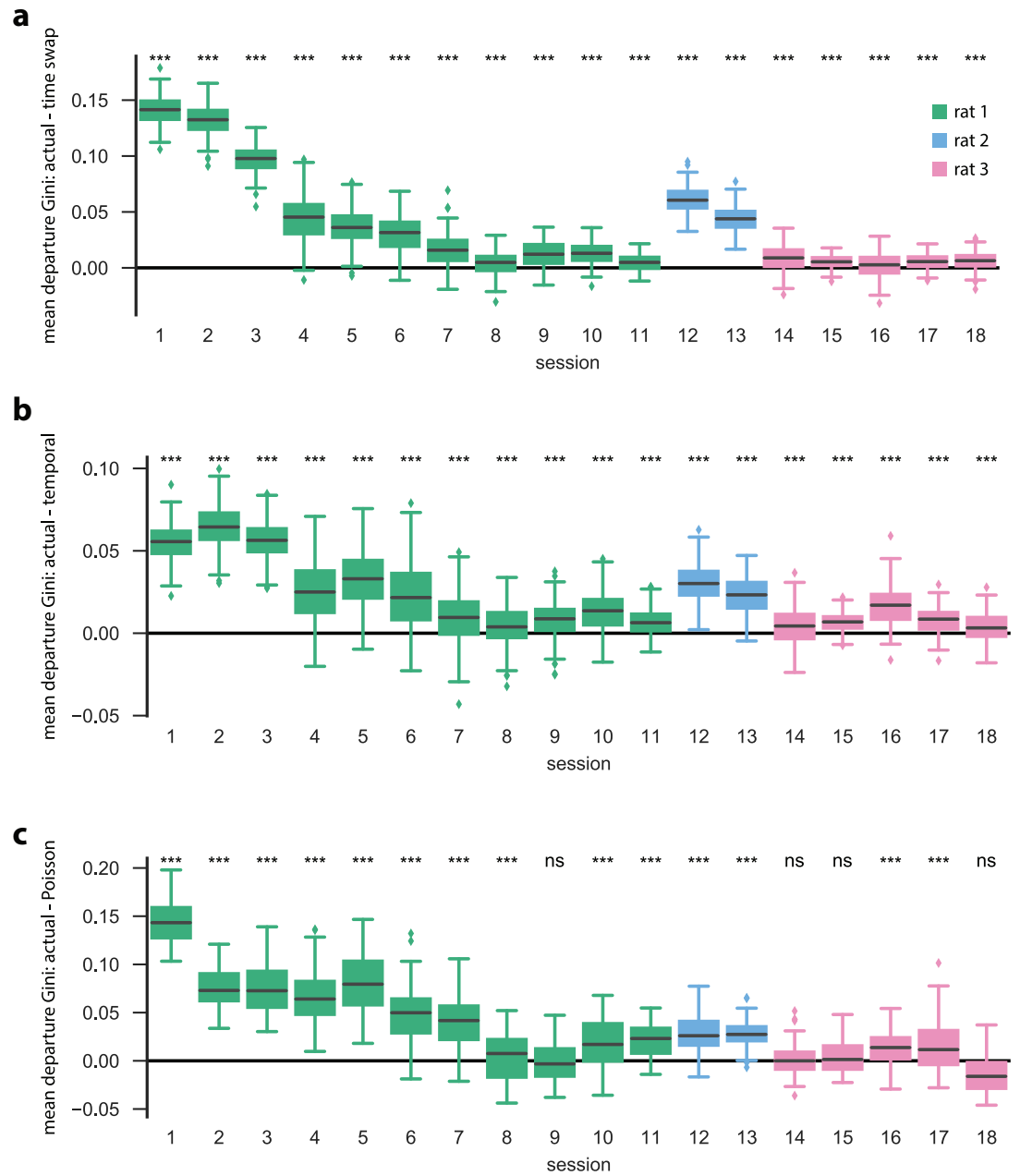
Figure 2–Figure supplement 1. We trained HMMs on neural activity during PBEs (in 20 ms bins), and asked how sparse the resulting state transitions were. In particular, we calculated the Gini coefficient for each row of our state transition matrix, so that the Gini coefficient for a particular row reflects the sparsity of state transitions from that state (row) to all other states (so-called "departure sparsity"). A high (close to one) Gini coefficient implies that the state is likely to only transition to a few other states, whereas a low (close to zero) Gini coefficient implies that the state is likely to transition to many other states. For each transition matrix, we computed the mean departure sparsity for $n = 250$ initializations, and for $n = 250$ shuffled counterparts for each of the surrogate datasets (**a.** time-swap shuffle, **b.** temporal shuffle, **c.** Poisson surrogate), and in each case we show the difference between the actual test data, and the surrogate test data. The actual data are significantly more sparse than both the temporal and time-swap surrogates for all sessions ($p < 0.001$, Mann–Whitney U test) and significantly more sparse than the Poisson surrogate for 14 of the 18 sessions ($p < 0.001$, Mann–Whitney U test).

853
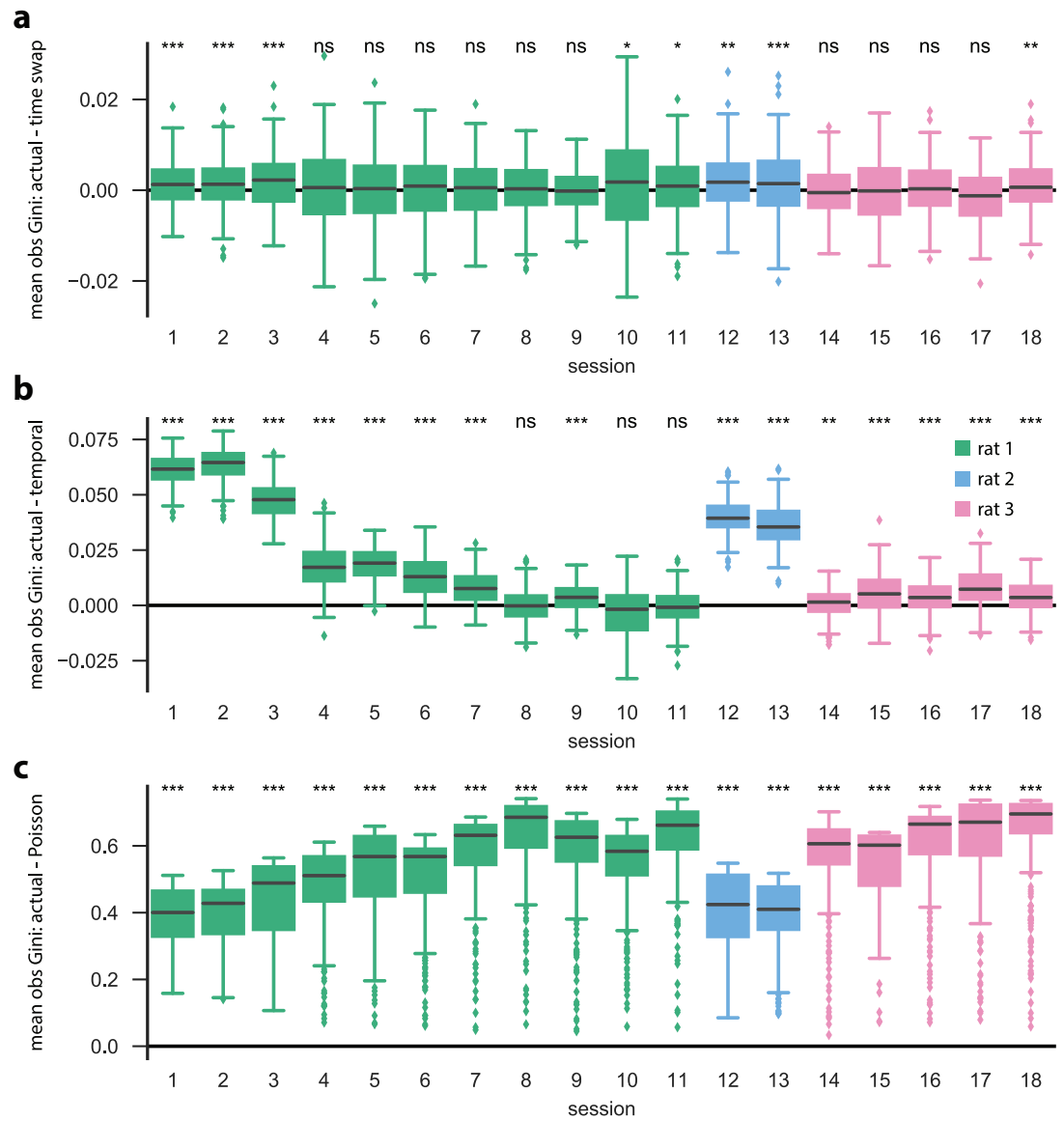
Figure 2–Figure supplement 2. Using the same PBE models and surrogate datasets ($n = 250$ shuffles each) as in *Figure 2–Figure Supplement 1*, we investigated the sparse participation of neurons/units in our models by calculating the Gini coefficient of each row (that is, for each unit) of the observation matrix. A high Gini coefficient implies that the unit is active in only a small number of states, whereas a low Gini coefficient implies that the unit is active in many states. For each initialization / shuffle, we calculate the mean Gini coefficient over all units, and the differences between those obtained using actual data and those obtained using surrogate data are shown: differences between actual and **a.** time-swap, **b.** temporal, and **c.** Poisson surrogates. We find that the actual data are significantly more sparse than the temporal and Poisson surrogates for most of the sessions ($p < 0.001$, Mann–Whitney U test), but that for many (10 out of 18) sessions, there is no significant difference between the mean row-wise observation sparsity of the actual data compared to the time-swap surrogate. This is an expected result, since the time-swap shuffle leaves the observation matrix largely unchanged.
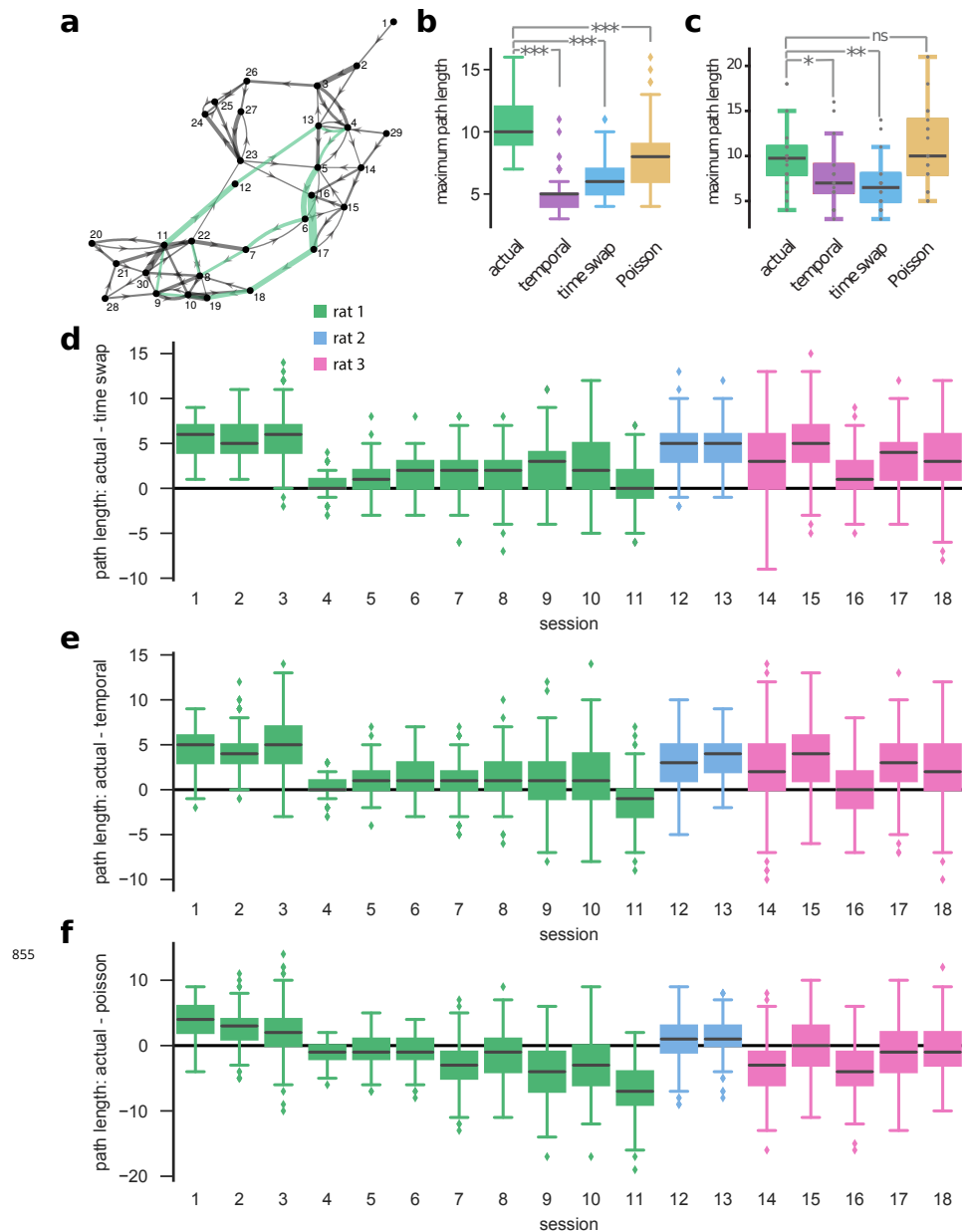
Figure 2–Figure supplement 3. We calculated the longest path within an unweighted directed graph corresponding to the transition matrices of HMMs, with nodes representing states and edges reflecting the transition probabilities (see Materials and Methods). **a.** The graph—displayed using the "force-directed layout" (*Fruchterman and Reingold, 1991*)—represents a model trained on actual data. For illustration purposes, we ignored transition probabilities below 0.1. The green path shows the longest path in the example. **b.** For this example session, we computed the maximum path length (the number of nodes in the longest path) for actual and corresponding shuffle datasets (temporal, time-swap, and Poisson) ($n = 250$ initializations / shuffles). **c.** The panel shows aggregate results built of median maximum path lengths from all sessions. We find that the actual data results in longer paths compared to time-swap ($p = 0.008$, Mann–Whitney U test) and temporal surrogate datasets ($p = 0.04$, Mann–Whitney U test). On the contrary, no significant difference is found in comparison with the Poisson datasets ($p = 0.57$, Mann–Whitney U test). Nevertheless, due to non-sparseness of the observation matrix for a Poisson model (*Figure 2–Figure Supplement 2*), in most instances these paths correspond to highly overlapping ensemble sequences. In panels **d–f**, difference between maximum path lengths obtained from actual data and surrogate datasets are shown separately for all sessions : actual versus **d.** time-swap, **e.** temporal, and **f.** Poisson. The data results in longer paths compared to time-swap and temporal shuffle datasets in most sessions (15 out of 18) ($p < 0.001$, Mann–Whitney U test), though in only five sessions compared to Poisson surrogate datasets.
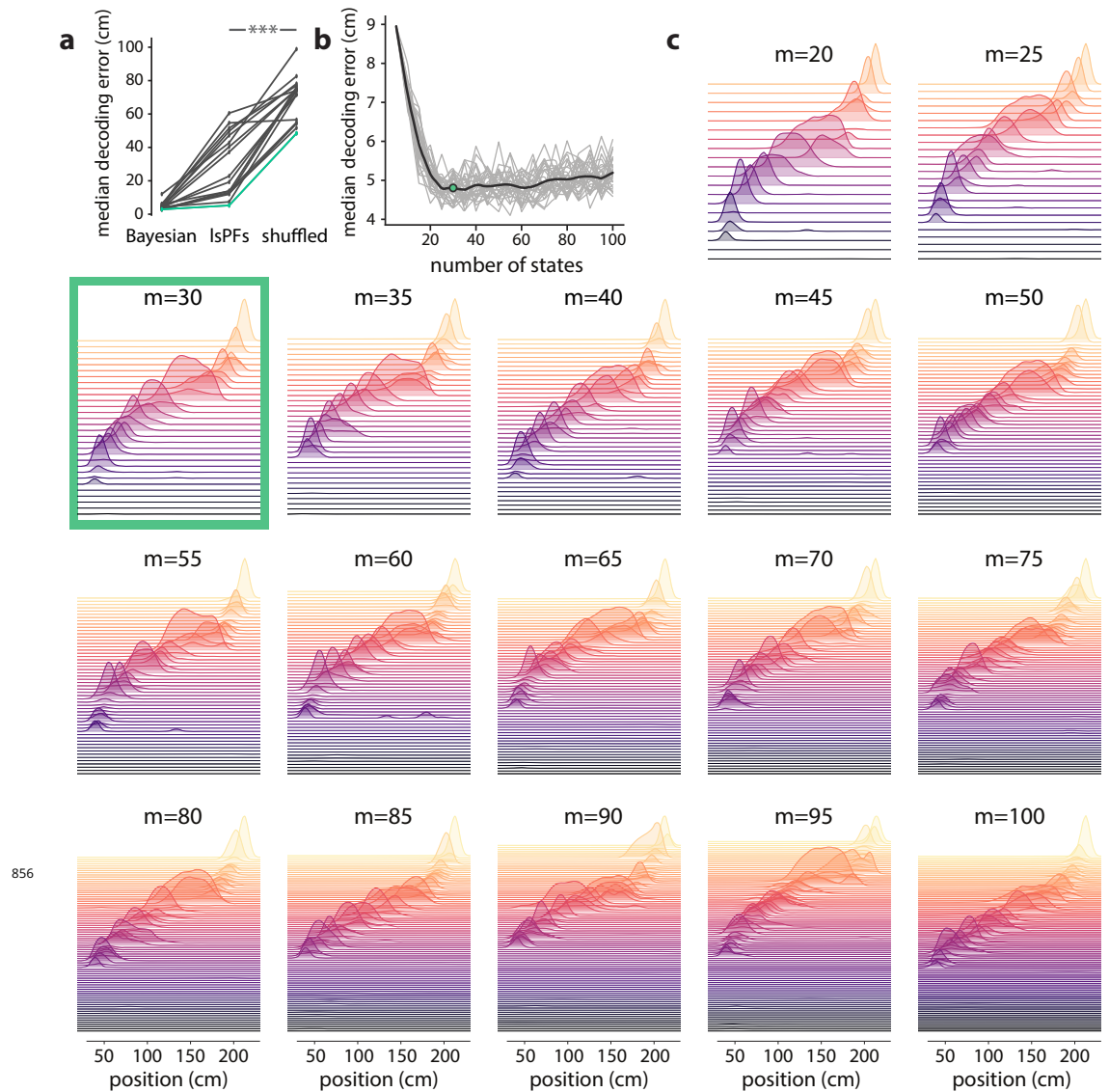
Figure 3–Figure supplement 1. We investigated to what extent our PBE models encoded information related to the animal's positional code by learning an additional mapping from the latent-state space to the animal's position (resulting in a latent-space place field, lsPF), and then using this mapping, we decoded run epochs to position and assessed the decoding accuracy. **a.** We computed the median position decoding accuracy (via the latent space) for each session on the linear track ($n = 18$ sessions) using cross validation. In particular, we learned a PBE model for each session, and then using cross validation we learned the latent space to animal position mapping on a training set, and recorded the position decoding accuracy on the corresponding test set by first decoding to the state space using the PBE model, and then mapping the state space to the animal position using the lsPF learned on the training set. The position decoding accuracy was significantly greater than chance for each of the 18 sessions ($p < 0.001$, Wilcoxon signed-rank test). **b.** For an example session, we calculated the median decoding accuracy as we varied the number of states in our PBE model ($n = 30$ realizations per number of states considered). Gray curves show the individual realizations, and the black curve shows the mean decoding accuracy as a function of the number of states. The decoding accuracy is informative over a very wide range of number of states, and we chose $m = 30$ states for the analysis in the main text. **c.** For the same example session, we show the lsPFs for different numbers of states. The lsPFs are also informative over a wide range of number of states, suggesting that our analyses are largely insensitive to this particular parameter choice (the number of states). The coloration of the lsPFs is only for aesthetic reasons.
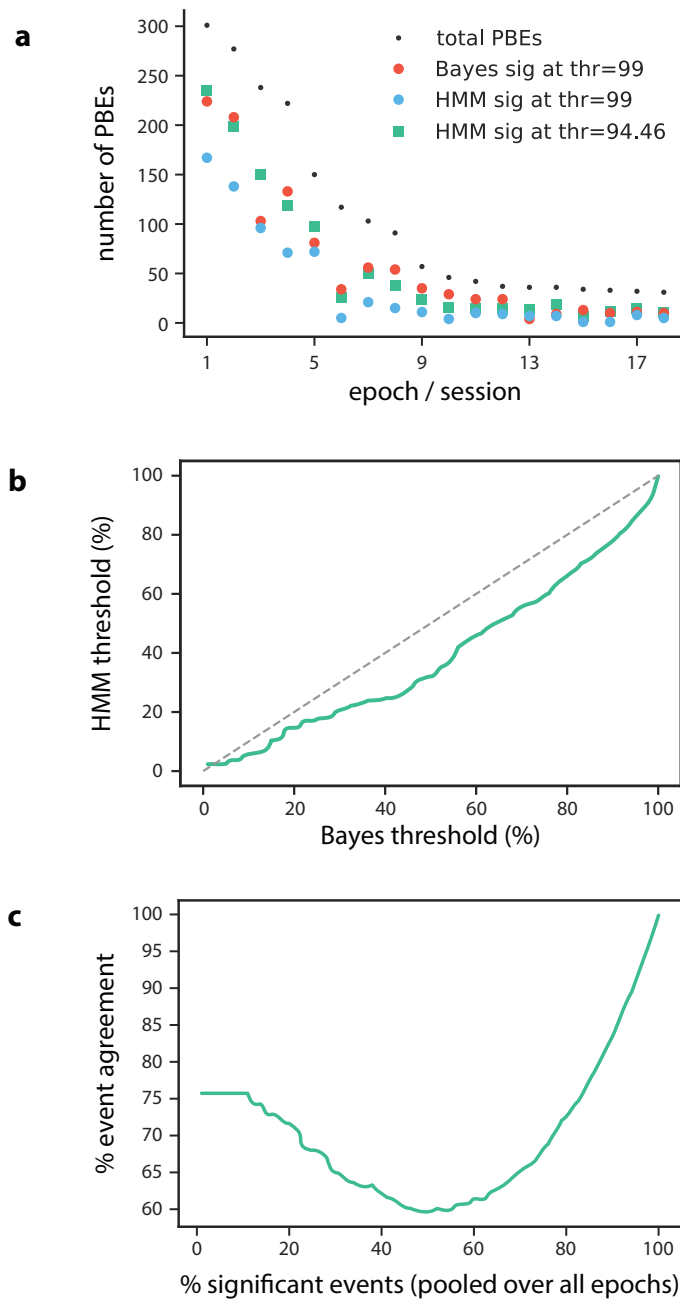
Figure 4–Figure supplement 1. a. The number of Bayesian significant PBEs, as well as the total number of PBEs are shown for each session ($n = 18$) when using a significance threshold of 99%. We find that 57% of PBEs (1064 of 1883) are Bayesian significant at this threshold. When using this same threshold for the model-congruence (HMM) significance testing, we find that only 35% of PBEs (651 of 1883) are model congruent. In order to compare the Bayesian and model-congruence approaches more directly, we therefore lowered the model-congruence threshold to 94.46%, at which point both methods had the same number of significant events (1064 of 1883). **b.** For each Bayesian significance threshold, we can determine the corresponding model-congruence threshold that would result in the same number of significant PBEs. **c.** Using the thresholds from **b.** such that at each point, both Bayesian and model-congruence approaches have the same number of significant PBEs, we calculate the event agreement between the two approaches. We note that our chosen threshold of 57% significant events has among the worst agreement between the two approaches.
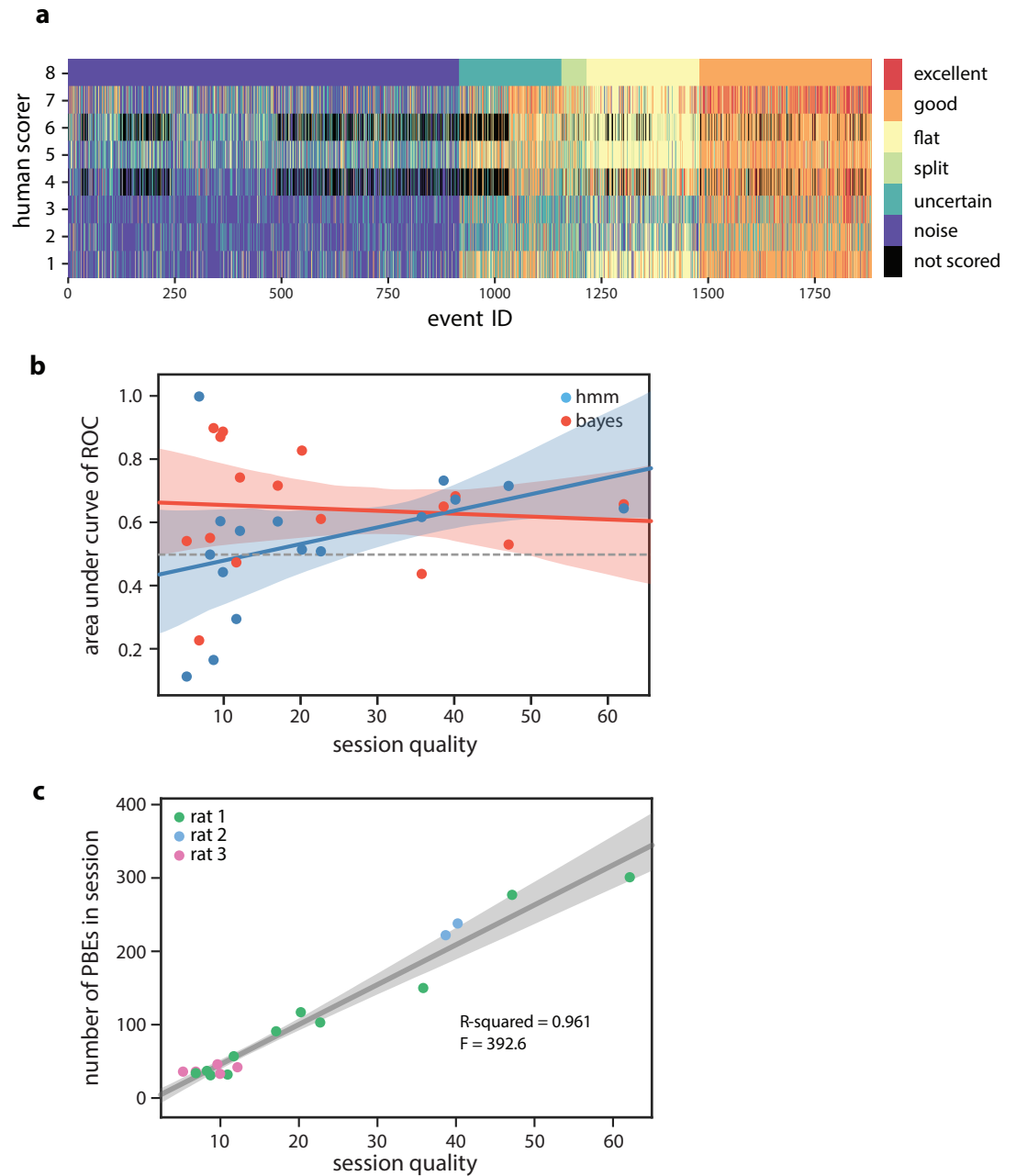
858

Figure 5–Figure supplement 1. a. Manual scoring results from 8 human scorers (six individuals scored $n = 1883$ events, two individuals scored a subset of $n = 1423$ events). Events were presented to each participant in a randomized order, and individuals were allowed to go back to modify their results before submission. Here, events are ordered according to individual #8's classifications. **b.** The model-congruence (HMM) approach appears to have higher accuracy when the session quality is higher ($R^2 = 0.17$, $F = 2.9$), which is consistent with our expectation that we need many congruent events in the training set in order to learn a consistent and meaningful model. **c.** The session quality is strongly correlated with the number of PBEs recorded within a session ($R^2 = 0.96$, $F = 392.6$).
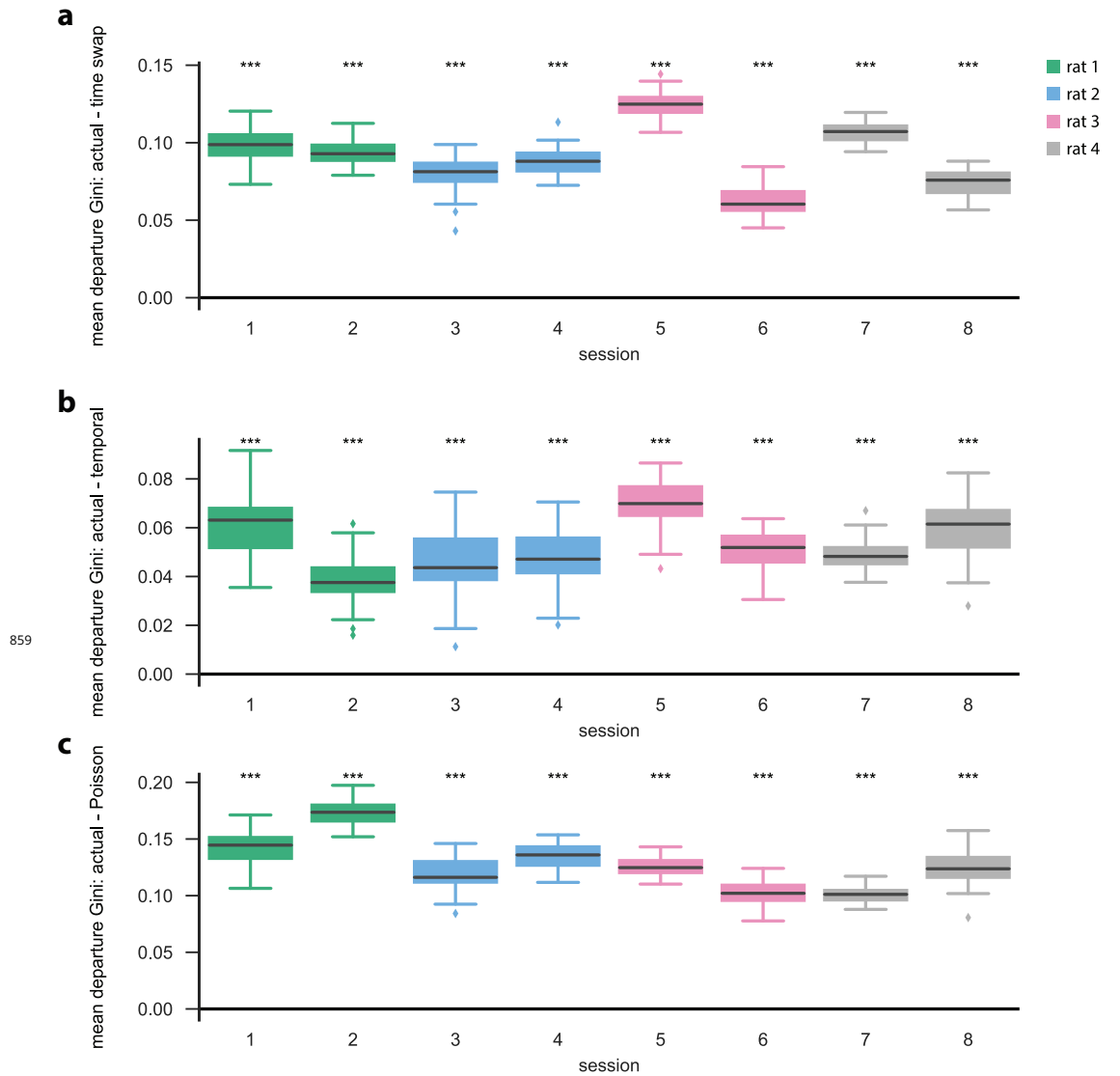
Figure 6–Figure supplement 1. Similar to the linear track (one dimensional) case, we find that models learned on actual open field PBE data are significantly more sparse (here showing mean departure sparsity) than their shuffled ($m = 50$ shuffles) counterparts. This is true for each of the $n = 8$ open field sessions ($p < 0.001$, Mann–Whitney U test). **a.** Difference [in departure Gini coefficients] between actual and time-swap test data, **b.** between actual and temporal test data, and **c.** between actual and Poisson surrogate data.
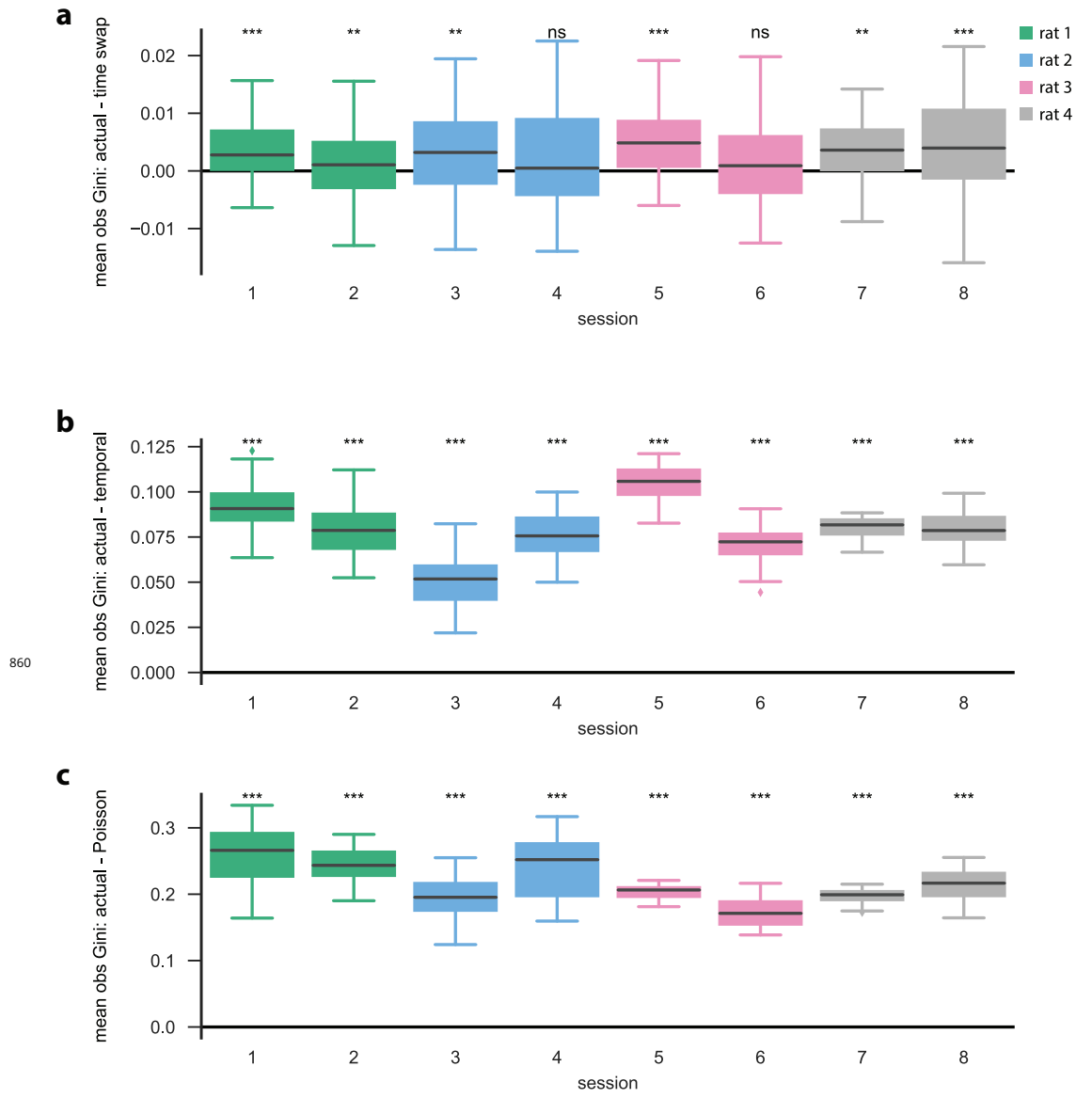
Figure 6–Figure supplement 2. a. Difference [in observation sparsity Gini coefficients across states] between actual and time-swap test data, **b.** between actual and temporal test data, and **c.** between actual and Poisson surrogate data. Similar to the linear track (one dimensional) case, we find that the observation sparsity across states for actual data are significantly greater than that of both the **b.** temporal and **c.** Poisson surrogates (for each session, $p < 0.001$, Mann–Whitney U test), and that **a.** for some sessions, there are no significant differences between the actual and time-swap surrogates.
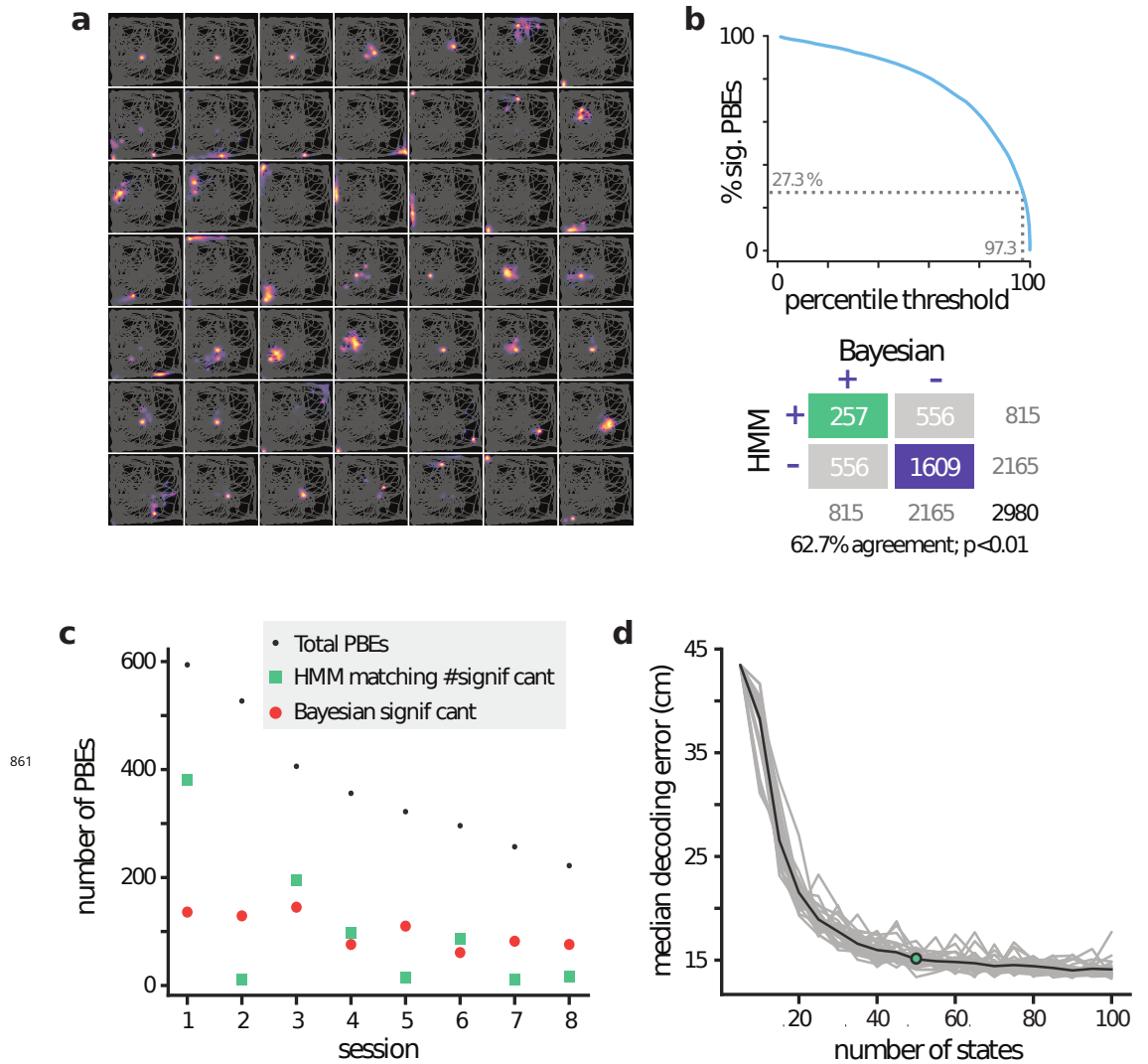
Figure 6–Figure supplement 3. a. lsPFs for 49 of the 50 latent states from an example session. **b.** (Top) Effect of model-congruence threshold on the number of significant PBEs. (Bottom) Comparison matrix between Bayesian replay detection and our model-congruence approach, where the threshold was chosen to match the total number of significant events pooled over all 8 sessions. **c.** Comparison between number of significant Bayesian events vs number of significant events using our model-congruence approach, when choosing the threshold as in **b.**. Sessions are ordered in decreasing numbers of total PBEs. Note that session 1 is a significant outlier, causing mismatches between many other sessions (2, 5, 7, 8), suggesting that matching on a per-session basis may be more appropriate in this case. **d.** Median position decoding error (via the latent space and lsPFs) was evaluated using cross-validation in an example session ($n = 30$ realizations for each model considered, shown in gray, mean shown in black), indicating that (i) the PBE-learned latent space encodes underlying spatial information, and (ii) that our PBE models are informative about the underlying position over a wide range of numbers of states.
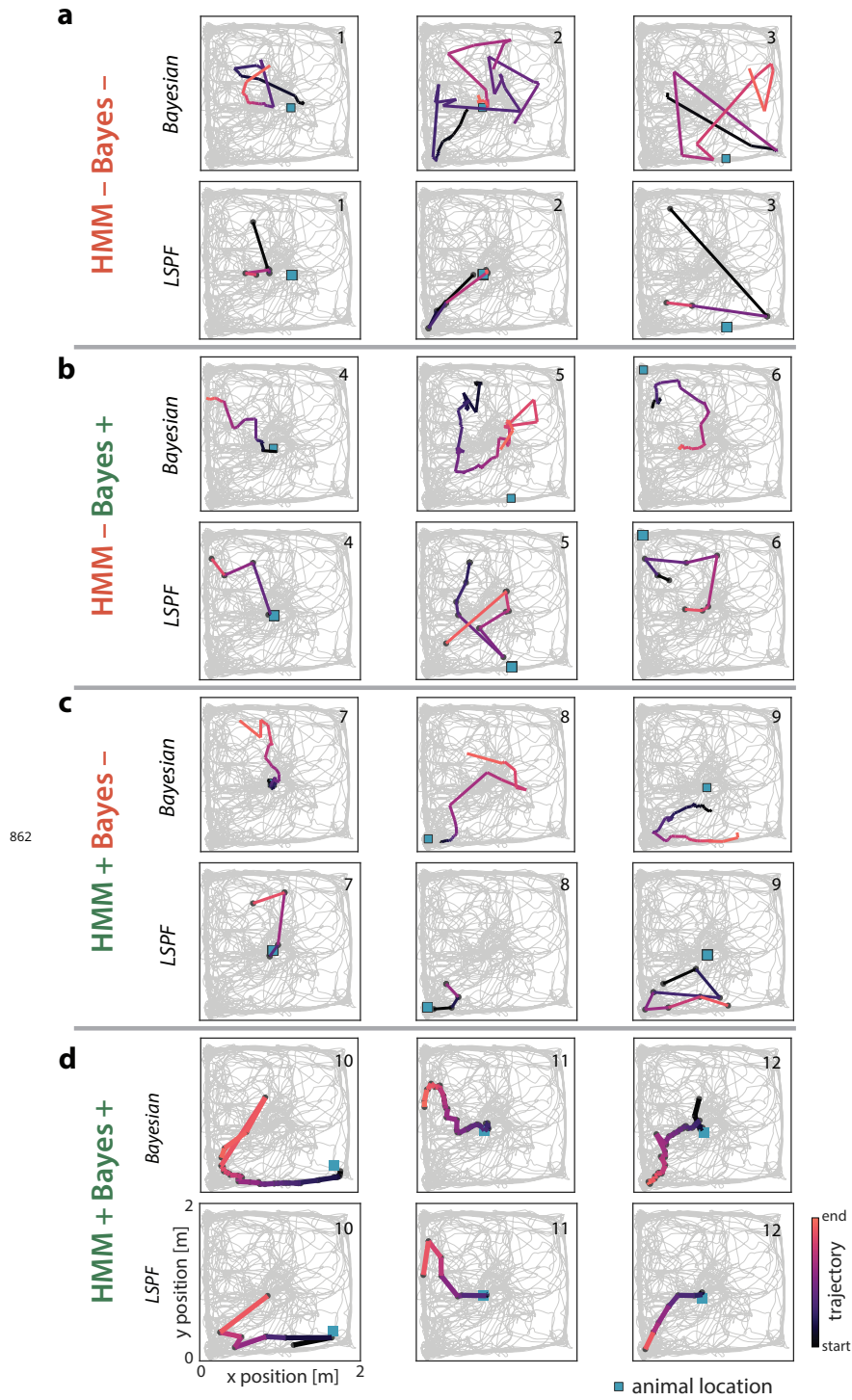
Figure 6–Figure supplement 4. a. Three example PBEs are shown that were classified as non-significant by both the Bayesian and model-congruence approaches. The top row shows the PBEs decoded with place fields using a Bayesian decoder in 20 ms bins, with a 5 ms stride. The bottom row shows the same events, but decoded in 20 ms non-overlapping time bins using the lsPFs. **b.** Three example PBEs are shown that were classified as significant replay by the Bayesian approach, but not by the model-congruence approach. **c.** Three example PBEs are shown that were classified as significant replay by the model-congruence approach, but not by the Bayesian approach. **d.** Three example PBEs are shown that were classified as significant by both approaches.